Chapter 2
Current Imaging Approaches and Challenges in the Assessment of the Intracranial Vasculature

Justin E. Vranic and Mahmud Mossa-Basha

Luminal Imaging Basics

Luminal imaging is a vascular imaging technique that evaluates the caliber of the intracranial vasculature. In some instances, these techniques can also provide information regarding the hemodynamics through vessels of interest. Conclusions regarding underlying vessel pathophysiology are ultimately drawn from the observed luminal irregularity and alterations in flow. Catheter digital subtraction angiography (DSA) is typically performed in a dedicated biplane neuroangiography suite. Before diagnostic images can be taken, intra-arterial access must be first acquired and a vessel(s) of interest must be selectively catheterized. Images are then acquired with high temporal resolution as a bolus of contrast flows through the vasculature of interest. CTA is a noninvasive luminal imaging modality that requires intravenous administration of iodinated contrast prior to image acquisition. Modern CT scanners rely on a multi-detector array for photon detection and image acquisition. Multiplanar reformats are subsequently derived from source data with high spatial resolution [1]. MRA techniques allow for the assessment of the vessel caliber and, in some instances, flow characteristics through intracranial vasculature. MRA acquisitions can be performed with or without intravenous contrast. Contrast-enhanced (CE) MRA relies upon the T1 shortening effects of paramagnetic contrast

J. E. Vranic
University of Washington, Department of Radiology, Seattle, WA, USA
e-mail: justedv@uw.edu

M. Mossa-Basha (✉)
University of Washington, Seattle, WA, USA
e-mail: mmossab@uw.edu

C. Yuan et al. (eds.), *Vessel Based Imaging Techniques*,
https://doi.org/10.1007/978-3-030-25249-6_2

media for luminal visualization [2]. Non-CE-MRA relies upon the intrinsic signal characteristics of flowing blood for luminal visualization. Noncontrast techniques specific to neurovascular imaging include time-of-flight (TOF), phase-contrast (PC), and arterial spin labeling (ASL) MRA.

Technical Aspects of Luminal Imaging

Conventional CTA

Conventional CTA requires the intravenous administration of iodinated contrast prior to image acquisition. A total bolus volume of 45–120 mL of contrast infused at a rate of 3–6 mL/s is generally sufficient for diagnostic quality image acquisition [3–5]. Contrast bolus monitoring techniques are commonly utilized to ensure that image acquisition is performed while the intracranial arteries are sufficiently opacified with contrast. Modern multi-detector CT (MDCT) scanners commonly possess an array of 64- or more detector panels, allowing for the acquisition of submillimeter thick image slices [1]. From this submillimeter thick source data, multiplanar reformats, maximum intensity projections, and 3D volume renderings can all be reconstructed with the goal of aiding in vascular lesion detection and characterization (Fig. 2.1a, b). Despite the improvements made in spatial resolution, conventional CTA continues to have inferior spatial and temporal resolution when compared to catheter DSA [6].

Catheter Digital Subtraction Angiography (DSA)

Catheter DSA (Fig. 2.2) image acquisition requires intra-arterial infusion of contrast into catheter-selected arteries. Contrast volumes ranging from 8 to 20 mL are frequently injected at flow rates ranging from 2 to 6 mL/s per diagnostic run, depending on the size of the intracranial vessel [3]. A range of frame rates for image acquisition can be used depending on the cerebrovascular pathology in question. Commonly, a frame rate of 3–6 frames per second provides adequate temporal resolution for the identification and assessment of rapid arteriovenous shunting. In some instances, frame rates as high as 60 frames per second or more can be acquired, providing superb temporal resolution. However, this comes at the cost of significantly increased radiation exposure to the patient. Modern biplane angiography units allow the operator to use highly customizable imaging projections to optimize visualization of the vessel or vascular lesion in question. The use of three-dimension rotational angiography (3DRA) allows for three-dimensional image acquisition of a specific vessel or vascular lesion. This cerebral angiography technique allows for thorough assessment of the vessel in question and is vital to accurate intervention planning.

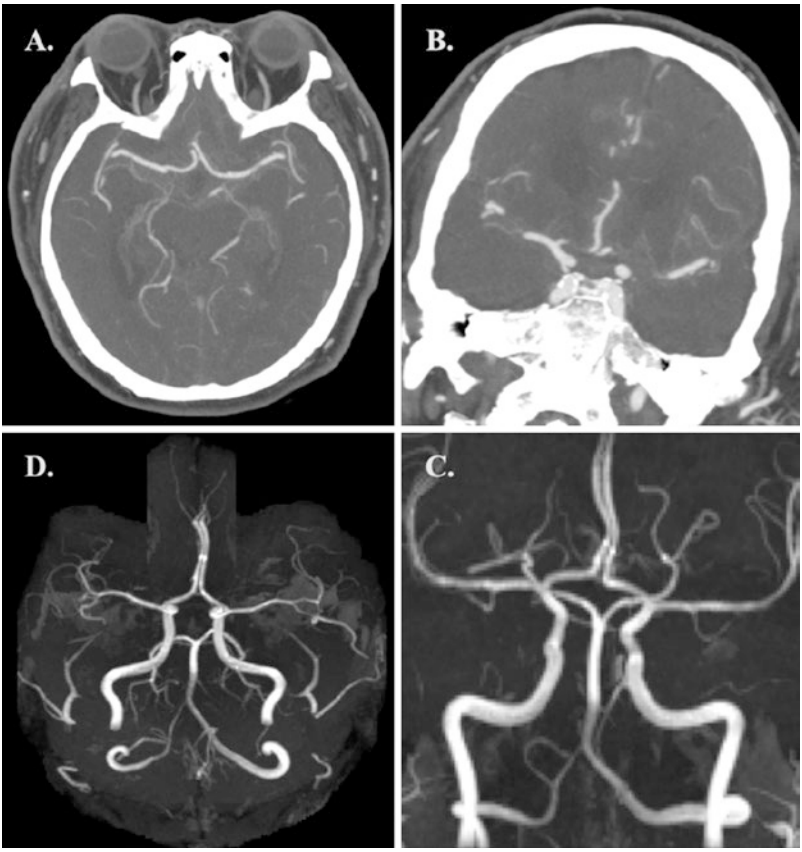

Fig. 2.1 (**a**, **b**) Axial and coronal CTA MIP images demonstrating normal intracranial vasculature. (**c**, **d**) Coronal and axial 3D-TOF-MRA MIP images demonstrating normal intracranial vasculature

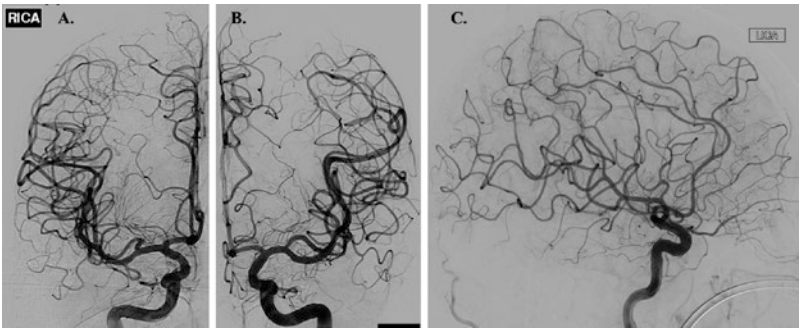

Fig. 2.2 (**a**, **b**) Frontal DSA images of the right and left ICA, respectively, illustrating normal intracranial vasculature. (**c**) Lateral DSA image of the left ICA again demonstrating normal intracranial vasculature

Dual-Energy CTA (DE-CTA)

Dual-energy CT (DE-CT) takes advantage of differences in x-ray attenuation by target materials. These differences in attenuation are dependent upon the energy of the incident photons [7]. The attenuation of materials with a high atomic number is greater with lower energy incident photons than with higher energy incident photons [7]. Similarly, the attenuation of blood vessels is more conspicuous when a low tube voltage is used [7, 8]. When an object of unknown composition is imaged with two distinct energy spectra, materials within the object can be differentiated by comparing the change in differential x-ray attenuation to the x-ray attenuation of known reference materials [7].

There are three DE-CT systems currently available. These include dual-source dual-energy CT (DSDE CT), single-source dual-energy CT (SSDE CT) with fast kilovolt-peak switching, and single-source dual-layer detector CT systems [9, 10]. DSDE CT uses two x-ray tubes that operate at different voltages (80 kVp and 140 kVp) positioned at 90° from each other [10]. In this system, spectral filtration can be independently optimized for each tube-detector pair, thus improving image quality. Due to differences in tube positioning relative to the target, acquisition of the two different datasets occurs at slightly different times, limiting the temporal registration of the DSDE CT images. Because both tubes are simultaneously energized, scattered radiation from one tube may be detected by the detector panel of the other tube (and vice versa), leading to degradation in spectral separation. Implementation of an appropriate scatter-correction algorithm can help correct for this phenomenon [10].

SSDE CT with fast kilovolt-peak switching relies on fast switching between 80 and 140 kVp performed every 250 microseconds during a single projection for spectral separation. This results in the acquisition of 1000 high-energy and 1000 low-energy projections during a single 360° gantry rotation at a full field of view of 50 cm. Unlike DSDE CT, SSDE CT with fast kilovolt-peak switching produces well-preserved spectral separation, and temporal misregistration of the spectral datasets rarely occurs. SSDE CT with a dual-layer energy detector relies on spectral separation at the level of the detector. A layered detector separates low-energy photons collected by the innermost detector layer from high-energy photons collected by the outermost detector layer from a single x-ray source [10].

Acquisition of low-energy monochromatic images with DE-CT allows for improved vessel contrast on CTA. These low-energy monochromatic images prove particularly helpful in delineating small, peripheral vessels [10]. Although the use of a low tube voltage with a traditional single-energy CT scan can produce similar effects, this comes at the cost of increased image noise which is not encountered with DE-CT. Additionally, acquisition of low-energy monochromatic images allows for the use of reduced iodinated contrast volumes while still preserving image quality [10]. This may prove helpful when imaging patients with underlying renal insufficiency in whom there is a clinical desire to minimize iodinated contrast exposure.

DE-CTA allows for the correction of beam-hardening artifact. Beam hardening arises when low-energy photons within a polychromatic x-ray beam are preferentially absorbed as they pass through a target [10]. This can result in streak on the reconstructed imaging and is frequently appreciated near the skull base and within the posterior cranial fossa. DE-CT corrects beam-hardening errors in the iodine- and water-based projection data, resulting in a reduction in beam-hardening artifacts and improved image quality [10].

Metallic implants produce significant streak artifact when imaged on a single-energy CT scanner. Monochromatic images obtained at higher energies with DE-CTA have increased penetration which reduces blooming and metallic streak artifacts [9, 10]. Image data collected at lower energies can then be used to correct for the decreased vessel contrast that occurs at these higher incident photon energies. The reconstructed image will display reduced metallic streak artifact with preserved vascular contrast. This technique proves particularly useful in evaluating vessel lumen patency following intraluminal stent placement. DE-CTA also allows for the subtraction of metallic artifacts, such as intracranial coil masses, from the reconstructed CTA images. This is accomplished through the subtraction of monochromatic images between the two energy levels obtained from the same datasets. In doing so, complete removal of objects with CT attenuation values that reach an upper threshold at both energy levels is achieved. Delineation of the parent vessel remains well-preserved on the subtracted monochromatic images [10]. This same technique can be applied to arterial wall calcifications and adjacent osseous structures, allowing for improved vessel lumen visualization [10–13].

Unlike conventional CTA, DE-CTA allows for reconstruction of virtual noncontrast images (VNC) from DE-CTA source data. Material subtraction images allow for the measurement of CT attenuation values on monochromatic images at 70 keV, which is equal to images acquired on a single-energy CT scanner at 120 kVp. VNC images allow for a reduction in overall radiation exposure, as separate scans acquired before and after contrast administration are no longer necessary [10].

4D-CTA/Timing-Invariant CTA (TI-CTA)

Four-dimensional CTA (4D-CTA), also referred to as timing-invariant CTA (TI-CTA), combines the noninvasive nature of conventional CTA with the dynamic imaging capabilities of catheter DSA [14]. 4D-CTA provides information regarding both the magnitude and directionality of flow through vessels of interest. It also details the angioarchitecture of the vasculature in question [14].

Like catheter DSA, a contrast bolus is delivered intravascularly and then imaged in real-time as it flows through the vasculature of interest. There are three distinct image acquisition techniques for performing 4D-CTA. These include volume mode, toggling-table mode, and shuttle mode scanning. The width of the CT detector ultimately determines which acquisition mode can be used to ensure adequate brain coverage [15].

Volume mode acquisitions are the most versatile, allowing for complete or partial coverage of the intracranial circulation. CTA data can be acquired either continuously throughout a pre-specified time period or discontinuously at either preset fixed or variable time intervals. During discontinuous volume mode acquisitions, the time intervals typically range from 1 to 4 seconds [15]. The datasets obtained at each of these time intervals are then overlaid to produce the final dynamic images [14]. True 4D datasets from continuous volume mode acquisitions can then be retrospectively reconstructed at any time interval. In general, the temporal resolution for this technique is on the order of 0.275–0.5 seconds [15]. Continuous scanning is only possible with volume mode acquisitions. Patients with high-flow vascular malformations benefit from the high temporal resolution of continuous acquisitions. When assessing collateral flow following arterial occlusion, a lower temporal resolution may be used, making the other acquisition techniques viable alternatives [15, 16].

4D-CTA images can be reconstructed from CT perfusion (CTP) datasets. In CTP, multiple CT datasets are acquired at different time intervals following the injection of intravenous contrast. Because 4D-CTA images can be reconstructed from CTP datasets, CTA imaging performed in addition to CTP imaging is not necessary, saving both time and radiation exposure [17]. By reconstructing 4D-CTA from CTP data, it is possible to evaluate both the angioarchitecture of the vasculature in question and the associated cerebral perfusion. The combination of these imaging techniques allows for the comprehensive assessment of the cerebral collateral vessels and the parenchymal perfusion that they supply [17–22].

Maximum intensity projections (MIPs) constructed from the 4D-CTA datasets provide an accurate overview of the vasculature of interest. Bone subtraction post-processing techniques can be used to generate DSA-like images that can be viewed as a temporal sequence that shows the arterial inflow and venous washout of contrast. By filtering the data in the temporal domain, spatial resolution remains intact, while noise is reduced, allowing for TI-CTA reconstructions of the vascular tree [15].

Time-of-Flight MRA (TOF-MRA)

TOF-MRA relies on suppression of background signal by slice-selective gradient echo excitation pulses [2, 24, 33]. In the selected slice or volume, static tissue experiences a rapid series of radiofrequency pulses that cause the tissue to lose most of its T1 signal. Inflowing blood, however, has not experienced these radiofrequency pulses and enters the slice or volume fully magnetized demonstrating a stronger T1 signal relative to the saturated background [24]. Saturation radiofrequency pulses are applied downstream of the slice or slab to suppress inflowing venous spins. Arterial contrast depends upon a combination of the T1 signal of both the arterial blood and background tissue, the radiofrequency pulse spacing and flip angle of the gradient echo sequence, and the velocity of the inflowing blood [33]. TOF-MRA

can be acquired in 2D or 3D formats, with 3D TOF-MRA being more suitable for imaging the intracranial arteries [2] (Fig. 2.1c, d). Three-dimensional acquisitions allow for isotropic voxels with submillimeter slice resolution [33]. Three-dimensional TOF-MRA is associated with longer image acquisition times, however, as well as increased susceptibility to flow dephasing artifacts resulting in loss of flow-related signal [2].

Multiple overlapping thin slab acquisition (MOTSA) is a hybrid of 2D TOF-MRA and single-slab 3D TOF-MRA that produces isotropic voxels with high spatial resolution and allows for larger anatomic areas of coverage [2, 34]. Overlapping subvolumes are sequentially acquired, before then being fused with other subvolumes to create a complete 3D volume [2].

First-pass Contrast-Enhanced MRA (CE-MRA)

First-pass CE-MRA images are commonly acquired using a T1W 3D gradient echo sequence [23, 24]. Artery visualization relies on the T1 shortening effects of intravenously delivered paramagnetic contrast agents, which makes the arteries of interest appear bright on imaging [2]. Suppression of background signal is achieved by the application of a 3D radiofrequency spoiled gradient sequence [2, 24].

First-pass CE-MRA depends upon appropriate contrast bolus concentration and timing to optimize vessel visualization. The volume of contrast required is dependent upon the magnetic field strength used, with lower concentrations and smaller volumes of contrast required when imaging is performed at higher magnetic field strengths. The contrast injection rate determines the arrival time of contrast at the vascular bed of interest. A fast injection ensures a tight bolus of contrast arriving over a short period; however, if the rate of infusion is too rapid, infusion-related artifacts can result. Optimal arterial visualization can generally be achieved using a double dose of contrast (0.2 mmol/kg) infused over a slower rate (2 mL/s) [2].

Standard extracellular contrast media are commonly used for first-pass CE-MRA and provide strong and selective enhancement of the vessels of interest [25, 26]. During the steady state, however, rapid contrast-agent extravasation occurs, resulting in decreases in the vessel contrast-to-noise ratio (CNR) and increased background signal within the surrounding soft tissues [25]. Consequently, these agents have a relative short distribution phase half-life of approximately 100 seconds [18], limiting the time available for image acquisition. Agents such as Gd-DTPA (Magnevist) and Gd-BOPTA (MultiHance) fall into this category.

Unlike standard extracellular contrast media, blood pool agents (BPA) demonstrate a prolonged intravascular distribution, allowing for strong and prolonged intravascular enhancement [25]. BPA provide an increased time frame for image acquisition (up to 60 minutes) and make steady-state MRA with high spatial resolution possible [27, 28]. BPA demonstrate significantly higher signal intensity in prestenotic and post-stenotic vessel segments [27], and MRA performed with BPA has

demonstrated superior image quality of the intracranial vasculature compared to standard extracellular contrast agents [18].

These agents can be divided into three broad categories which include ultrasmall supraparamagnetic iron oxide (USPIO) particles, paramagnetic gadolinium-based macromolecules, and gadolinium-based small molecules with strong reversible protein binding. Of these three classes, USPIO particles and gadolinium-based small molecules with strong reversible protein binding prove to be the most clinically promising. USPIO particles demonstrate strong T1 and T2 shortening effects and are retained within the intravascular space for prolonged periods of time. On T1W imaging, these particles appear bright. Sequences with short echo times are necessary to minimize confounding susceptibility artifacts [25]. Examples of USPIO particles include ferumoxtran-10 (Combidex, Sinerem, Guerbet, France), ferumoxytol (Advanced Magnetics, USA), and SHU-555C (Supravist) (Bremerich 2007). These agents have not yet received FDA approval for clinical use. Although paramagnetic gadolinium-based small molecule agents, such as gadofosveset trisodium (Vasovist/Ablavar), have received FDA approval for use in humans, they are no longer made commercially available by their manufacturers.

First-pass CE-MRA requires the appropriate timing between contrast bolus infusion and image acquisition. The scan time delay between contrast agent infusion and the start of imaging acquisition can be approximated using the following formula [2]:

$$\text{Scan Time Delay} = \text{Contrast Travel Time} + \left(\text{Injection Time} / 2\right) - \left(\text{Scan Time} / 2\right)$$

This formula does not take into account reduced cardiac output, high-grade arterial stenoses, or abnormal shunt vascularity [2]. A contrast test bolus of 1–2 mL that is injected at the same rate as the actual injection can be used to determine the contrast travel time [2]. From this, the appropriate scan delay can be deduced. Automated bolus detection represents an alternative method for coordinating contrast bolus delivery and image acquisition [23]. This technique involves monitoring a vessel of interest for the arrival of contrast. Once an adequate contrast volume is within the vessel, image acquisition is initiated [2].

Optimization of image acquisition parameters is essential to acquiring high-quality angiographic images. Repetition time (TR) should be kept as short as possible (<4 ms) without increasing the bandwidth [2, 24]. By decreasing TR, it is possible to perform multiphase imaging or increase image spatial resolution. As TR is shortened, however, the signal-to-noise ratio (SNR) subsequently decreases. This can be compensated for by increasing the rate of contrast infusion [2, 24]. Like TR, echo time (TE) should also be kept as short as possible (<2 ms). A shortened TE decreases proton dephasing which in turn reduces the loss of intravascular signal [2]. This can also decrease SNR by widening the readout bandwidth. TR, TE, and SNR are each affected by changes in the readout bandwidth, with a high readout bandwidth allowing for shorter TR and TE at the expense of SNR. A readout bandwidth of 32–64 kHz is generally sufficient for CE-MRA. The flip angle typically ranges from 20 to 60° in the case of CE-MRA with most image acquisitions utilizing a flip

angle between 30 and 45° [2]. Low flip angles are better suited for low contrast doses, slow injection rates, and very low TR, whereas high flip angles are better for high contrast doses and imaging with higher TR.

Increasing the magnetic field strength increases SNR which can be used to increase spatial resolution, decrease image acquisition time, or reduce contrast dose [2, 24]. A 3T field strength causes a T1 prolongation of tissue. Subsequently nonvascular tissues with longer T1 relaxivities are more readily suppressed with 3T scanners [24]. Increased magnetic field strength also increases the specific absorption rate (SAR) and generates higher field inhomogeneities when compared to 1.5T. Increased SAR limits the maximum flip angle that can be used, thereby limiting the increase in SNR. Despite these technical limitations, the net gain in signal remains higher at 3T when compared to 1.5T [2].

Time-Resolved Contrast-Enhanced MRA (TR-CE-MRA)

TR-CE-MRA represents a unique form of CE-MRA that provides important temporal information in addition to structural information about angioarchitecture. TR-CE-MRA acquires image sets sequentially at multiple time points during the passage of contrast through vessels of interest [30]. TR-CE-MRA provides high temporal resolution while maintaining sufficient SNR and spatial resolution, allowing for the evaluation of hemodynamic flow and distinction between arterial and venous structures [2]. Precise bolus timing is not necessary with TR-CE-MRA as multiple vascular phases are obtained [2]. Three-dimensional volume acquisitions are possible, providing greater anatomic coverage and higher spatial resolution and SNR [2]. TR-CE-MRA image acquisition techniques include keyhole imaging; contrast-enhanced time-robust angiography (CENTRA); time-resolved imaging of contrast kinetics (TRICKS; GE Healthcare, Chicago, IL); time-resolved echo-shared angiographic technique (TREAT); time-resolved imaging with stochastic trajectories (TWIST; Siemens Healthineers, Erlangen, Germany) (Fig. 2.3); four-dimensional (4D) time-resolved angiography using keyhole (4D-TRAK); vastly undersampled isotropic projection (VIPR); and highly constrained back-projection reconstruction (HYPR) [2, 31].

Keyhole imaging generates a series of images by combining rapidly acquired temporal samples of the central k-space region before performing a single sampling of the outer regions of k-space at the end of the scan [2, 31]. Although this technique provides some sense of the flow dynamics through vessels of interest, high spatial frequency venous signals appear even in the early arterial frames due to late high spatial frequency sampling [31]. CENTRA imaging relies on randomly segmented k-space ordering in which a central sphere of k-space is randomly sampled during the full arterial window. Acquisition of data can extend beyond the time of passage of the contrast bolus through the arteries so that high spatial resolution of a large field of view is achieved [2].

TRICKS imaging samples the center of k-space more frequently than the periphery, and time frames are formed by temporal interpolation [2, 31]. K-space is sub-

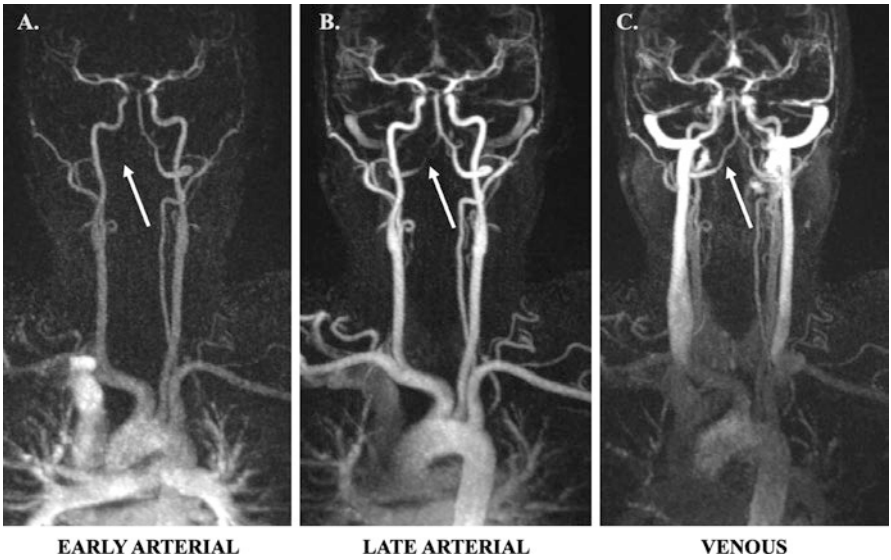

Fig. 2.3 (**a**) Coronal TR-TWIST-MRA acquired during the early arterial phase shows opacification of the pulmonary vasculature, aorta, and the major aortic branch vessels. Although the carotid arteries and left vertebral artery are well visualized, the right vertebral artery is not opacified (arrow). (**b**) A late arterial phase image shows delayed partial opacification of the right vertebral artery (arrow). (**c**) Venous phase image shows increased delayed opacification of the right vertebral artery (arrow). This patient was found to have a right vertebral artery dissection with impaired flow through the vessel. Non-time-resolved MRA techniques could have led to an erroneous diagnosis of vertebral artery occlusion

divided into fixed portions, and a part of the peripheral k-space is updated for every keyhole dynamic. Additionally, a rectangular keyhole is used to acquire full lengths of k-space lines [24]. The TRICKS technique then attempts to estimate missing k-space data by linear interpolation of values from shared data across time frames [30]. TRICKS increases the frame rate of a 3D multiphase examination by a factor of 3–4 [2]. This technique offers a significant improvement over the keyhole method because of the ongoing updating of high spatial frequency information. This technique and subsequent derivate methods are the most prevalent commercially available methods for TR-CE-MRA. Although frames may be updated every few seconds, the data used to form each frame covers a substantial time interval of 10 seconds or more due to the temporal interpolation that is required [31].

Multiple variations of the TRICKS technique exist, each with its own unique name. The main differences between these techniques are the size of the central k-space portion that is sampled and how it is combined with k-space periphery data [24]. Like TRICKS, the TREAT technique uses a rectangular keyhole to acquire full lengths of k-space lines with alternating lines of k-space being sampled with each iteration [32]. The TWIST technique alternates between sampling central and peripheral k-space using a spiral, pseudostochastic trajectory. This trajectory is based on the radial distance from the center of k-space and partially updates the k-space periphery

[24, 32]. 4D-TRAK combines the CENTRA technique with sensitivity encoding (SENSE), partial Fourier, and keyhole techniques [2]. A central keyhole ellipsoid of k-space is acquired at each successive dynamic time point, and the periphery of k-space is acquired at the last dynamic time point. The k-space periphery acquired at the end of the scan is then used to reconstruct all of the previous dynamics where only the central keyhole was acquired, ultimately optimizing the speed with which contrast enhancement is captured [24]. 4D-TRAK allows for more than 60-times accelerated MRA with high spatial resolution [2, 24]. Temporal resolutions of 1.6–3 seconds can be achieved within the intracranial vasculature [2]. The temporal performance of dynamic high-resolution 3D TR-CE-MRA is faster than what can be achieved by conventional first-pass CE- or non-CE-MRA techniques [2].

Phase-Contrast MRA (PC-MRA)

PC-MRA generates image contrast by exploiting inherent differences in transverse magnetization that occurs between stationary and moving tissues, resulting in phase shifts [2]. PC-MRA uses a flow-encoding gradient along multiple planes to visualize flow [2, 24]. Gradients are turned on in one direction at a time for a pre-specified time interval before then being switched in orientation for the same amount of time. The first gradient dephases spins, while the second gradient rephases spins that are stationary. After application of this bipolar gradient, stationary spins associated with background tissue will have a zero phase shift, whereas spins associated with the flowing intravascular blood pool will accumulate a net phase shift that can then be visualized [24, 33]. This phase shift is proportional to the flow velocities within the imaged vessels [2] with higher flow velocities accumulating more phase shift. Velocity-induced phase shift can subsequently be quantified [2, 35].

PC-MRA requires preselection of a velocity-encoding factor (Venc) based on whether faster moving arterial blood or slower moving venous blood will be imaged [2]. Appropriate Venc selection is critical to image quality. If the Venc is too low, velocity aliasing occurs, whereas if the Venc is too high, vascular CNR will be too low due to decreased sensitivity to slow flow near the edge of the vessel lumen [2, 24, 33]. A reference image is acquired in addition to the velocity-encoded scan. The reference image can then be subtracted from the flow-sensitive images to remove phase errors unrelated to flow. Because phase shift is proportional to flow velocity, an image can be generated where pixel intensity directly relates to flow velocity [24].

Arterial Spin Labeling MRA (ASL-MRA)

ASL-MRA labels flowing spins within the blood pool for image generation. ASL-MRA requires that two image sets are acquired and later subtracted for final image generation. These two image sets differ only in the magnetization of inflowing

arterial spins. Pseudocontinuous labeling techniques can also be utilized. In this variant, a stream of radiofrequency energy is applied to a thin (~1 cm thick) labeling plane through which intravascular arterial spins flow before traveling downstream into the vasculature of interest. Pseudocontinuous ASL (pCASL) improves the SNR of vessels near the labeling plane. ASL-MRA allows for high arterial contrast and complete elimination of background signal. The use of extended, multiphase readouts can provide time-resolved ASL data as illustrated by triggered angiography noncontrast-enhanced (TRANCE) MRA (Philips Healthcare; Best, Netherlands) [33].

Clinical Considerations for Luminal Imaging

Catheter DSA

Catheter DSA has superior spatial and temporal resolution when compared to noninvasive, cross-sectional luminal imaging modalities, making it well-suited for the detection of small cerebrovascular lesions, such as blister aneurysms of the supraclinoid ICA, small AVMs, and small dural arteriovenous fistula (dAVF). DSA has been shown to better characterize geometric features of aneurysms, including the width and conformation of the aneurysm neck, when compared to CTA and MRA [36]. Traditionally, DSA has been used to assess changes in the intracranial vasculature following open surgery, endovascular intervention, or radiation therapy. Because intra-arterial access is required to perform DSA, examinations can be easily converted into therapeutic endovascular procedures, such as endovascular aneurysm coiling or parent artery reconstruction, should the need arise.

Catheter angiography is an invasive procedure with associated iatrogenic risks. The most serious of these complications is catheter-associated embolic phenomena capable of producing transient or permanent focal neurological deficits. The risk of transient focal neurological deficits following cerebral angiography is estimated to be 0.9%, whereas the risk of permanent neurological deficit is lower, estimated to be 0.5% [6, 37–40]. Arterial wall dissection is also possible. Puncture site complications include perivascular hematoma, arterial pseudoaneurysm formation, arteriovenous fistula formation, and vessel occlusion. The risk of clinically significant perivascular hematoma requiring either surgical evacuation or blood transfusion is approximately 0.2%. The risk of arterial injury or arterial occlusion requiring surgical thrombectomy or thrombolysis is approximately 0.2% [41].

Catheter angiography exposes both patients and operators to radiation. The dose of radiation that one receives increases with increasing frame rate of image acquisition. An individual's cancer risk is proportional to increases in radiation exposure [6, 42, 43]. Unlike noninvasive luminal imaging, catheter angiography requires the coordination and participation of multiple other clinical providers, including dedicated neurointerventionalists and their associated support staff. This makes catheter angiography a time- and resource-intensive endeavor relative to CTA and MRA.

2D DSA projections can limit detection of subtle vascular lesions due to vessel overlap. In these instances, dedicated 3D rotational angiography (3DRA) acquisitions are helpful in further evaluating a region of interest. Despite catheter angiography's superb spatial and temporal resolution, it does not allow for direct visualization of soft tissues, including the vessel wall. Clinically relevant information regarding vessel wall characteristics such as abnormal wall thickening, atherosclerotic plaque burden and composition, vessel wall inflammation, and the presence of intramural hematoma or intraplaque hemorrhage remain largely unknown when catheter angiography is used to assess the intracranial vasculature. In the case of ICAD, catheter DSA can significantly underestimate plaque burden as plaque remodeling often occurs in an outward fashion early in the disease process without appreciable luminal stenosis.

Conventional CTA

The combination of high spatial resolution, short image acquisition time, and the noninvasive nature of conventional CTA makes it an ideal screening examination, particularly in critically ill individuals or in the emergency department setting where efficient patient triage and throughput is essential to overall departmental function. As such, a patient's clinical stability is less of a concern when it comes to CTA image acquisition. Critically ill patients are often able to complete both noncontrast head CT and CTA image acquisitions without issue.

Compared to DSA, there is little short-term risk to patients in performing CTA. Like DSA, iodinated contrast is utilized in CTA imaging protocols. While rare, allergic reactions occur in approximately 0.2–0.7% of patients exposed to intravenous low-osmolar iodinated contrast media. The majority of these reactions are nonlife-threatening [44]. Like contrast-induced allergic reactions, contrast-induced nephropathy is also considered a rare clinical entity that is most likely to occur in patients with poor baseline renal function, though this topic is controversial [45–48] and some question the existence of post-contrast acute kidney injury. Nonetheless, caution should still be exercised in patients with ordered CTA exams who have severely compromised renal function but continue to produce urine [45, 48–50].

CTA is of limited utility in the evaluation of intracranial vascular lesions following open surgical clipping, coil embolization, or endovascular flow diversion. This is due to significant metallic streak artifact generated by these implanted materials. CT imaging in general has difficulty evaluating the posterior cranial fossa and skull base secondary to beam-hardening artifact and photon starvation caused by the dense surrounding bone.

CTA has difficulty detecting small (<3 mm) aneurysms, including blister aneurysms, small bifurcation aneurysms, perforator artery aneurysms, dissecting aneurysms, and peripheral mycotic and myxomatous aneurysms [38]. CTA, with the exception of time-resolved or multiphase CTA, only provides a single time point of

imaging. This limits its ability to thoroughly evaluate vascular lesions that demonstrate shunting phenomena such as intracranial AVMs and dAVFs. Additionally, CTA provides limited information about pathological processes affecting the intracranial arterial walls. While findings such as eccentric narrowing of the vessel lumen may suggest ICAD, these findings are not accurate for vasculopathy differentiation.

DE-CTA

Relative to conventional CTA, DE-CTA can be used to improve vessel contrast, particularly as it relates to small and peripheral blood vessels. This proves particularly useful in the evaluation of the intracranial vasculature. The distinct high- and low-energy spectra generated by DE-CTA can be used to reduce beam-hardening artifact at the skull base and within the posterior cranial fossa. These spectra can also be used to minimize metallic streak artifact from objects such as aneurysm clips, endovascular coil masses, or endovascular flow diverters. DE-CTA can be used to reliably assess vessel patency following endovascular stent placement as well as to evaluate for residual aneurysm sacs following microsurgical clipping. This imaging modality is highly sensitive to parent vessel compromise and residual aneurysm sac formation following the placement of multiple aneurysm clips [9]. DE-CTA can produce VNC images from DE-CTA datasets which are helpful in assessing for intracranial hemorrhage and differentiating hemorrhage from iodinated contrast [10], potentially allowing for better prediction of hematoma expansion. Unlike conventional CTA where patients must be scanned before and after contrast delivery, DE-CTA requires only one scan from which VNC images can be reconstructed. This ultimately reduces patient radiation exposure.

Despite its many advantages, DE-CTA has several pertinent shortcomings. First, DE-CTA exposes patients to ionizing radiation. However, the total radiation dose for DE-CTA is estimated to be equivalent to or reduced relative to standard CTA imaging [7, 10, 12]. Although VNC images can be generated from DE-CTA datasets, they have more noise than conventionally acquired noncontrast head CT images. This image noise, however, does not appear to adversely affect radiologists' abilities to identify acute intracranial hemorrhage [22].

4D-CTA/TI-CTA

The clinical value of 4D-CTA comes from its ability to provide both vascular structural information and the associated flow characteristics, making it useful for the evaluation of flow patterns in acute stroke, Moyamoya disease, AVMs, dAVFs, and large intracranial aneurysms. Additionally, 4D-CTA can provide information regarding the relationship between intracranial tumors and pertinent arterial vascular supplies and venous drainage pathways that may be useful to surgical planning [14].

4D-CTA possesses several unique clinical advantages relative to other luminal imaging techniques. Good correlation exists between 4D-CTA and DSA for the detection and grading of intracranial high-flow vascular malformations [15, 16]. Retrograde cortical venous flow can be visualized with 4D-CTA [15]. 4D-CTA can more accurately grade collateral vascularity in the setting of acute ischemic stroke than conventional CTA [15, 20, 22].

4D-CTA uses ionizing radiation for image acquisition and therefore exposes patients to nontrivial amounts of radiation. Because multiple image acquisitions are performed, the cumulative radiation dose for 4D-CTA is significantly higher than conventional CTA [15]. Despite this fact, the cumulative radiation dose of 4D-CTA is likely still lower than that of catheter DSA [16]. 4D-CTA generates thousands of images as part of a single study. As such, significant computing power is necessary for fast and efficient image post-processing [15].

First-pass CE-MRA

First-pass CE-MRA is a useful imaging modality for the follow-up evaluation of coiled intracranial aneurysms [2]. Compared to noncontrast 3D TOF-MRA, first-pass CE-MRA is more sensitive to the presence of aneurysm neck remnants [51] and can more accurately classify these remnants [2]. The detection of aneurysm neck remnants with 3D TOF-MRA can be improved, however, by scanning with intravenous contrast [51]. Unlike non-CE-MRA techniques, first-pass CE-MRA is relatively insensitive to artifacts generated by turbulent flow and saturation effects [28].

Unlike other MRA techniques, first-pass CE-MRA requires accurate timing of contrast bolus arrival to ensure that the maximum volume of contrast is within the target vessel lumen at the time of scan initiation [2]. The accuracy of first-pass CE-MRA in detecting vascular lesions such as brain aneurysms is limited by the enhancement of adjacent venous structures if timing is delayed [2]. An obvious example of this is the presence of a cavernous segment ICA aneurysm that is surrounded by the cavernous sinus. After aneurysm coiling, the aneurysm wall may demonstrate thin peripheral enhancement which is postulated to represent some combination of peripherally distributed intra-aneurysmal thrombus, vasa vasorum within the adventitial layer of the aneurysm wall, and/or ingrowth of vascularized tissue about the coil mass due to inflammation or healing. Regardless of the underlying etiology, these findings may be confused with a residual aneurysm sac on all types of CE-MRA [51].

TR-CE-MRA

TR-CE-MRA provides a combination of structural and hemodynamic information about the intracranial vasculature. It provides for evaluation of the complex flow patterns of intracranial AVMs and dAVFs [2]. This technique facilitates the

visualization of arterial feeders, the nidus, and draining veins in AVMs [2, 52–54] and allows for the evaluation of dAVFs due to its sensitivity for the detection of early venous drainage [2].

TR-CE-MRA readily depicts vascular lesions with arteriovenous shunting [24, 30]. It can determine the directionality of flow through vascular structures and has excellent suppression of background tissue signal [24]. Unlike other luminal imaging modalities, TR-CE-MRA is relatively insensitive to the shape and timing of the contrast bolus [29]. The start of image acquisition coincides with the start of intravenous contrast injection, and no timing bolus is required [30].

TR-CE-MRA commonly exhibits a trade-off between spatial and temporal resolution, with greater temporal resolution coming at the expense of spatial resolution. Additional loss of SNR can result from the incorporation of acceleration techniques, such as parallel imaging. Blurring of vessel walls commonly occurs when aggressive undersampling is applied [32]. In consideration of the vascular disease being evaluated, balancing the spatial and temporal resolution and imaging acceleration for optimal disease evaluation is paramount.

TOF-MRA

TOF-MRA is routinely used to image the cervical and intracranial arteries. It provides a useful screening tool for asymptomatic patients at higher risk for cerebral aneurysm [33]. 3D TOF-MRA has proven particularly useful in imaging the intracranial vasculature due to its higher spatial resolution, whereas 2D TOF-MRA is typically reserved for evaluation of the cervical vasculature [55].

The scan time for TOF-MRA is longer than first-pass CE-MRA [56]. Signal loss of in-plane flow due to saturation effects can occur, giving the appearance of pseudostenosis or pseudo-occlusion. Signal loss occurs in vessels with complex or turbulent flow, as can be seen in areas of moderate- or high-grade vascular stenosis, large intracranial aneurysms, or arteriovenous malformations, secondary to intravoxel dephasing [55]. In the setting of arterial stenosis, dephasing artifacts can overexaggerate the degree of stenosis or even present a stenosis as an occluded artery [2].

PC-MRA

PC-MRA is an excellent imaging technique for the visualization of the intracranial veins, allowing for accurate detection of dural venous sinus thrombosis [2]. PC-MRA also offers excellent background signal suppression, improving visualization of the intracranial vasculature [33, 55].

The use of multiple flow-encoding gradients lengthens the scan time for PC-MRA relative to other non-CE-MRA techniques [2]. As with TOF-MRA, PC-MRA experiences signal loss in vessels with turbulent flow because of intravoxel dephasing.

This imaging artifact can lead to an overestimation of luminal stenosis [55]. PC-MRA is susceptible to patient motion because of mask subtraction that occurs as part of image generation [55]. PC-MRA image quality is largely dependent upon appropriate Venc parameters. Finally, PC-MRA image post-processing is complex, making it a time- and resource-intensive endeavor [56].

ASL-MRA

ASL-MRA is an imaging technique that provides complete suppression of background tissues, allowing for high-quality angiographic image generation with high CNR [33]. ASL-MRA is well-suited for imaging vascular regions with rapid flow such as the extracranial or intracranial carotid arteries [56].

ASL-MRA is associated with long image acquisition times, requiring two image acquisitions so that the signal from background tissues can be subtracted out of the final image set [33, 55, 56]. Because image subtraction is performed, ASL-MRA is sensitive to patient motion causing misregistration artifact [33, 56]. Like other non-CE-MRA techniques, in cases of slow flow, ASL provides decreased vascular coverage due to a combination of signal losses and the delayed arrival of spin-labeled protons [33]. This is particularly important in the setting of high-grade stenosis causing severe reduction in downstream flow velocities or in patients with poor cardiac output.

Luminal Imaging Characterization of Cerebrovascular Pathology

Intracranial Aneurysms

Intracranial aneurysms are pathological vessel wall outpouchings which can be located anywhere within the intracranial circulation but are commonly encountered at vessel bifurcation points. DSA better characterizes geometric and morphologic features of aneurysms, flow characteristics of aneurysms, as well as the lesion's relationship to the arterial vasculature and small branch origins when compared to CTA and MRA [36]. DSA has a higher sensitivity and specificity for the detection of small supraclinoid blister aneurysms which prove difficult to identify with either CTA or MRA. Additionally, DSA outperforms CTA in the detection of small dissecting aneurysms, perforator artery aneurysms, and small peripheral infectious or myxomatous aneurysms [38].

DSA allows for accurate aneurysm assessment following treatment with microsurgical clipping, endovascular coiling, or flow diversion. After such interventions, DSA accurately identifies residual aneurysm necks and incompletely thrombosed

aneurysm sacs [57] as well as identifies in-stent stenosis following flow diverter placement [57]. While the use of flow-diverting stents has posed many technical challenges to both conventional CTA and MRA evaluation, DSA has not encountered the same issues. Unlike these other luminal imaging modalities, DSA can accurately and reproducibly quantify the degree of in-stent stenosis following flow-diverter placement [58–60].

Information regarding aneurysm size, dome morphology, direction of dome projection, and location in the intracranial circulation can all be attained from CTA with a high degree of accuracy [61]. With conventional CTA, the sensitivity and specificity for aneurysm detection are more than 80% [62]. Unfortunately, CTA assessment of treated aneurysms proves significantly more difficult. Assessment of the aneurysm neck proves particularly difficult. The use of metallic streak artifact reduction techniques paired with iterative and noise-reduction filters is emerging as a promising CTA imaging technique for the evaluation of treated intracranial aneurysms [63].

Like CTA, MRA can also accurately characterize intracranial aneurysms (Fig. 2.4). 3D TOF-MRA demonstrates a sensitivity and specificity for the detection of intracranial aneurysms ≥3 mm that exceeds 80% [64]. First-pass CE-MRA using a 3D T1W gradient echo sequence with short TE and 3D TOF-MRA with contrast are accurate follow-up imaging modalities for the detection and surveillance of aneurysm recanalization after endovascular treatment [58]. These techniques can be used to reliably monitor intracranial aneurysms that have undergone stent-assisted coiling. In these patients, the presence of a stent in the parent artery at the aneurysm neck does not diminish the accuracy of CE-MRA in the detection of aneurysm remnants [58]. It is important to apply MRA with the shortest possible TE in order to limit metallic susceptibility artifact and prevent obscuration of a potential residual aneurysm lumen [51].

Intracranial Arteriovenous Malformations

Intracranial AVMs are abnormal clusters of blood vessels characterized by feeding arteries coalescing into a central nidus which drains directly into veins, bypassing intervening capillary beds (Fig. 2.5). While rare, these lesions are of high clinical significance given their propensity to bleed. In cases of intracranial AVMs, there is a 2–4% risk of spontaneous hemorrhage per year. Following sentinel bleeding episodes, these lesions have a rebleeding risk as high as 30% within the first year, depending on their location and venous drainage patterns [65]. Accurate identification of the AVM nidus, the abnormal feeding arteries, and the venous drainage pathways is critically important to appropriate management decisions and therapy planning [65–67]. DSA allows for accurate characterization of the angioarchitecture as well as characterization of associated perinidal and intranidal aneurysms which, when present, contribute to rupture risk and may affect lesion management [66].

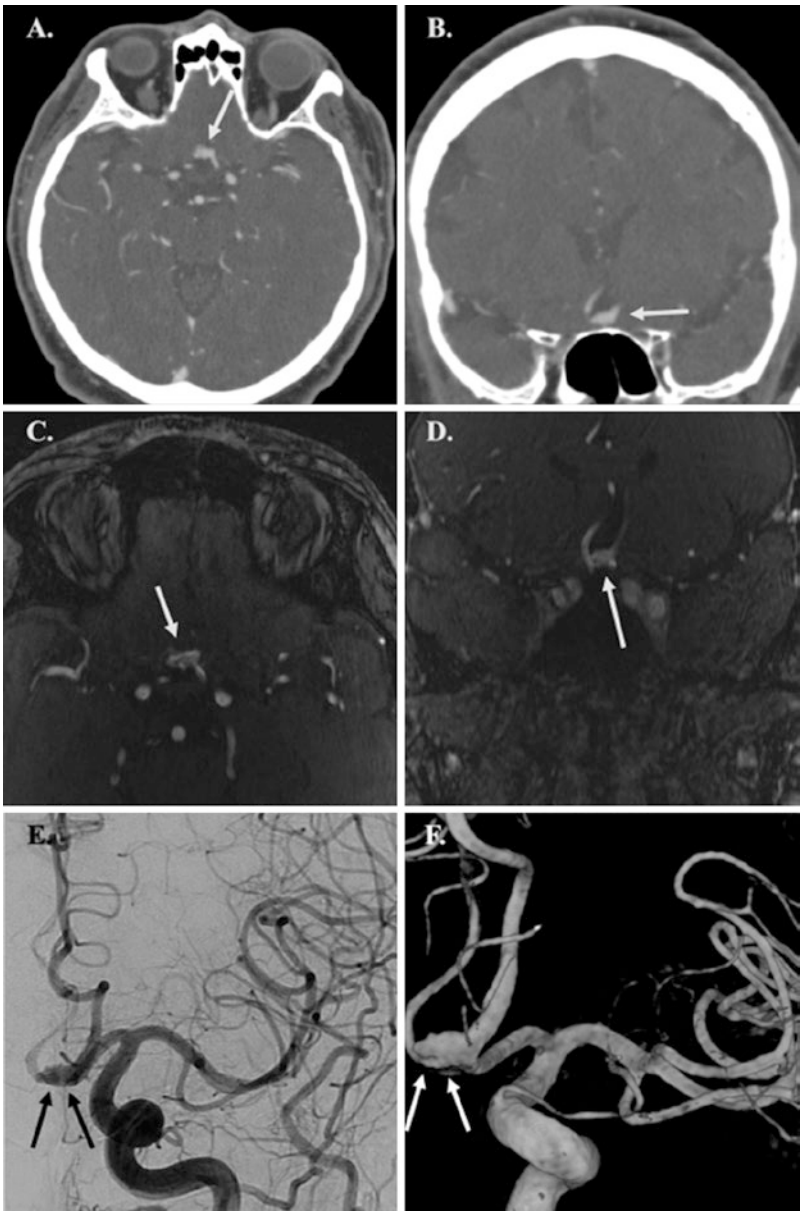

Fig. 2.4 (**a**, **b**) Axial and coronal CTA MIP images demonstrating a saccular aneurysm of the anterior communicating artery (arrows). (**c**, **d**) Axial and coronal 3D-TOF-MRA images again demonstrating a saccular aneurysm of the anterior communicating artery (arrows). (**e**) Frontal DSA projection again demonstrating the anterior communicating artery aneurysm (arrows) visualized on CTA and MRA. (**d**) 3D rotational angiographic image provides better visualization of the aneurysm (arrows). On this image, a focal bleb arising from the right side of the aneurysm sac and a small perforator vessel arising directly from the aneurysm dome are more conspicuous than on 2D DSA alone

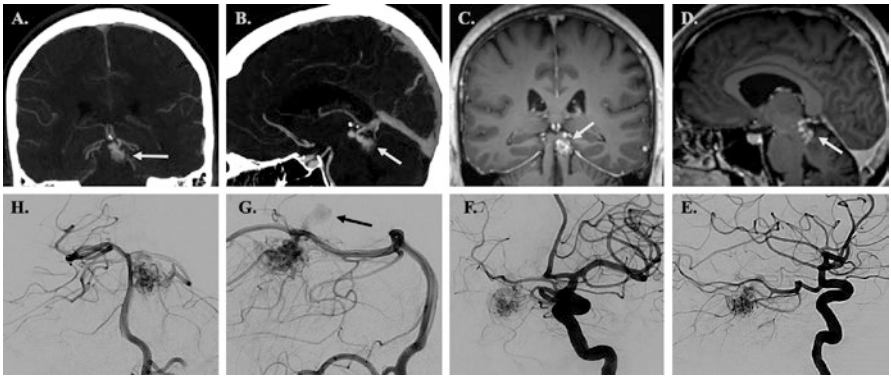

Fig. 2.5 (**a**, **b**) Coronal and sagittal CTA MIP images depicting a small AVM (arrows) within the left midbrain. (**c**, **d**) Coronal and sagittal MPRAGE images again showcasing this small AVM (arrows). (**e**, **f**) Lateral and oblique DSA images show a large left fetal posterior communicating artery supplying blood from the anterior circulation to the AVM nidus. (**g**, **h**) Lateral and transfacial DSA images of a left vertebral artery injection demonstrate a small AVM nidus in the left midbrain that is supplied by left PCA branches. Early faint opacification of a dilated venous varix representing early venous drainage is appreciated (black arrow in image **g**)

The overall sensitivity and specificity of CTA for the detection of underlying vascular anomalies following spontaneous intraparenchymal hemorrhage range from 83.6% to 100% and 77.2% to 100% [68, 69], respectively. When evaluating for only ruptured and unruptured intracranial AVMs, the sensitivity of CTA has been reported to be as high as 90% [70]. This sensitivity increases to more than 95% in cases of unruptured AVM detection. Conversely, the presence of intracranial hemorrhage decreases the sensitivity of CTA to approximately 87% [70]. The sensitivity of CTA for detecting AVMs is also dependent upon lesion size. Small AVMs prove more difficult to detect and evaluate than larger ones. Published reports suggest that the sensitivity of CTA decreases to approximately 60–84% when dealing with AVMs less than 3 cm in diameter [70]. CTA also allows for the identification and characterization of flow-related circle of Willis and perinidal and intranidal aneurysms [65]. Modern CTA has been shown to detect more than 85% of AVM-associated aneurysms [70].

Improvements in the temporal resolution of current TR-CE-MRA techniques have allowed for improved AVM characterization. Current TR-CE-MRA techniques can delineate arterial inflow and identify the AVM nidus [71] as well as increase diagnostic confidence [72]. Despite these improvements, accurate depiction of venous drainage remains difficult. Additionally, MRA generally performs poorly in the identification of flow-related perinidal and intranidal aneurysms [70]. DSA is typically required to both accurately characterize lesional venous drainage and confidently exclude perinidal/intranidal aneurysms following AVM detection with MRA or CTA.

Dural Arteriovenous Fistulas

Dural arteriovenous fistulae (dAVFs) are pathological anastomoses between meningeal arteries and dural sinuses or cortical veins (Fig. 2.6). They are distinguished from pial AVMs by their arterial supply and lack of a parenchymal nidus. The risk of adverse neurological events depends on the degree of dural sinus involvement and the presence of cortical vein reflux, with cortical vein reflux representing a known risk factor for hemorrhage. The pathophysiology underlying the development of these lesions is not well known; however, in a small subset of these lesions, head trauma, infection, tumor, dural sinus thrombosis, or prior craniotomy are favored to represent contributing factors for their formation [73].

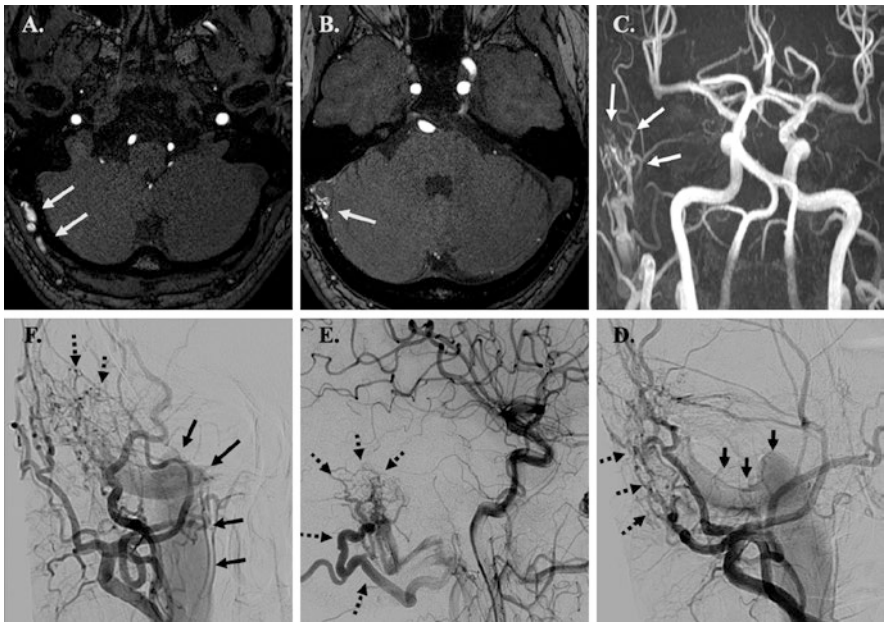

Fig. 2.6 (**a**, **b**) Axial 3D-TOF-MRA images showing dilated branches of the right occipital artery draining into the right sigmoid sinus (arrows) consistent with a dural AVF. (**c**) Coronal 3D-TOF-MRA MIP image showing asymmetrically hypertrophied extracranial vessels in the vicinity of the right sigmoid sinus (arrows). (**d**, **f**) Oblique, lateral, and frontal DSA images better illustrate the angioarchitecture of this dural AVF. The fistula is supplied by hypertrophied branches of the right occipital, posterior auricular, and middle meningeal arteries (dashed lines). Early venous drainage into a dilated right sigmoid sinus and internal jugular vein is also appreciated (solid black arrows). The high temporal resolution of DSA provides important hemodynamic information regarding flow through the lesion. Additionally, subtle cortical vein reflux that might otherwise be missed on CTA or MRA is more readily identified on DSA

Catheter DSA allows for accurate delineation of feeder artery anatomy, arteriovenous shunting, dural sinus and venous anatomy, and cortical vein reflux [65, 73, 74]. In addition to cortical vein reflux, catheter angiography identifies engorged leptomeningeal veins which are another imaging finding of venous congestion [73, 74]. Evaluation of dAVFs with CTA is difficult as these lesions often do not have a nidus. CTA features of dAVFs include the early opacification of a dural sinus, stenosis or thrombosis of a dural sinus, asymmetric enlargement of cortical veins, and the presence of enlarged medullary or pial veins [65, 75]. The presence of medullary or pial vein enhancement on CTA is reported to have the highest specificity for dural AVFs with associated cortical vein reflux with a specificity greater than 90% [75].

Historically, the evaluation of dAVFs with MRA was difficult given the lack of lesion nidus and the complex associated flow patterns. Technical improvements in TR-CE-MRA have made this technique a more viable imaging alternative for dAVF screening and evaluation [74]. Improvements in temporal resolution using techniques such as CENTRA k-space sampling have improved separation of arterial and venous phases, allowing for improved visualization of venous outflow [76]. In a small cohort, TRICKS-MRA has been shown to correctly identify (or exclude) and grade dAVFs relative to catheter DSA in more than 90% of cases [77].

Intracranial Vasculopathies

Intracranial vasculopathies represent an array of disease processes which affect the walls of intracranial arteries. These disease processes ultimately manifest as single or multifocal narrowing or irregularity on luminal imaging. These diseases include intracranial atherosclerotic disease (ICAD), reversible cerebral vasoconstriction syndrome (RCVS), infectious/inflammatory vasculitis, and Moyamoya disease (MMD). ICAD has a variety of appearances on luminal imaging. Early in the disease process, there is outward vessel wall remodeling with minimal or no luminal stenosis [78]. As ICAD progresses, eccentric luminal stenosis is frequently present [79–81]. ICAD most commonly involves arterial bifurcation points and more commonly involves proximal intracranial arteries (Fig. 2.7). Unlike ICAD, infectious/inflammatory vasculitis (Figs. 2.8 and 2.9) and RCVS will often present with concentric luminal stenoses that is thought to more commonly involve peripheral branches as compared to ICAD [81–83]. Luminal imaging features of RCVS include involvement of multiple vascular territories with a beaded appearance of medium to large cerebral vessels with multifocal areas of narrowing interspersed with normal caliber vessel segments [84]. RCVS may also present as diffuse luminal narrowing (Fig. 2.10). In cases of first-pass CE-MRA or 3D TOF-MRA with contrast, smooth concentric vessel enhancement may be appreciated at the site of stenosis in patients with underlying infectious/inflammatory vasculitis [85]. This enhancement is better visualized on dedicated vessel wall imaging (VWI) studies.

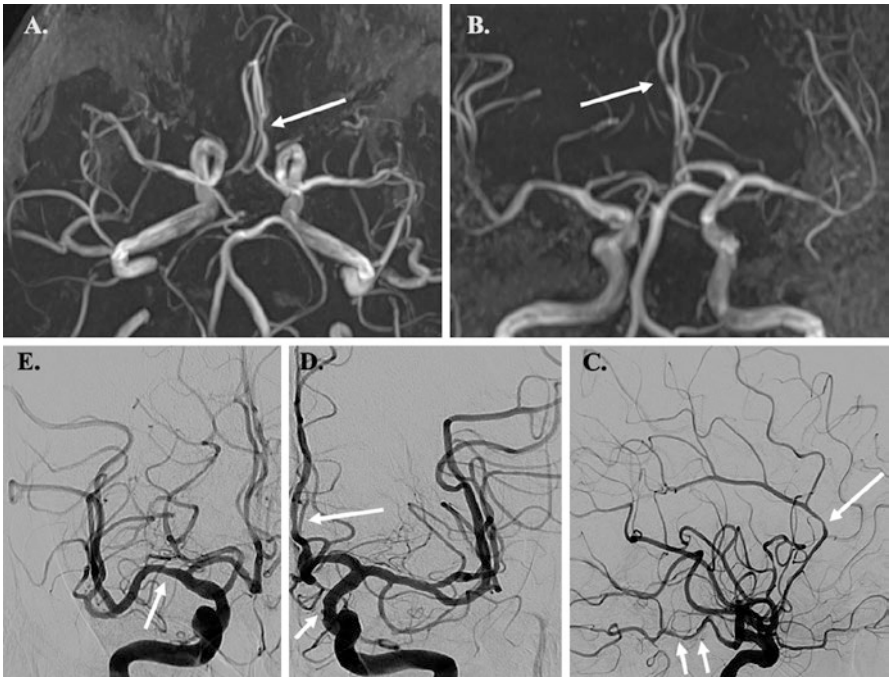

Fig. 2.7 (**a**, **b**) Axial and coronal 3D-TOF-MRA MIP images showing focal stenosis of the proximal left A2 segment (arrow). (**c**) Lateral DSA image of the left ICA highlights eccentric, multifocal narrowing of the left ACA and the left PCA (arrows). (**d**) Frontal DSA image of the left ICA shows eccentric narrowing of the supraclinoid ICA and proximal A2 segment (arrows). (**e**) Frontal DSA image of the right ICA with eccentric narrowing of the proximal M1 segment (arrow). The eccentric distribution of these multifocal stenoses within the proximal intracranial vasculature, closely associated with arterial branch points, is consistent with intracranial atherosclerotic disease (ICAD)

In the case of MMD, luminal imaging commonly demonstrates stenosis and occlusion of the carotid termini, proximal MCAs, and proximal ACAs with development of robust compensatory collateral vessels as the disease process progresses (Fig. 2.11), at least in the middle stages of disease evolution [80, 86]. True MMD commonly demonstrates concentric, smooth tapering until occlusion, whereas MMS caused by ICAD is more likely to have irregular occlusion and will more frequently involve other vascular territories with irregular, multifocal narrowing, although MMD may also involve the posterior circulation [86]. While MMD does not have to involve both sides equivalently at the time of detection, the patient will eventually develop bilateral steno-occlusive disease. This is not the case with many MMS processes. There is frequently proximal collapse of the ipsilateral cervical internal carotid artery in MMD secondary to downstream outflow obstruction.

Luminal imaging, such as DSA, provides information regarding the severity and distribution of luminal stenoses in patients with an underlying intracranial vascu-

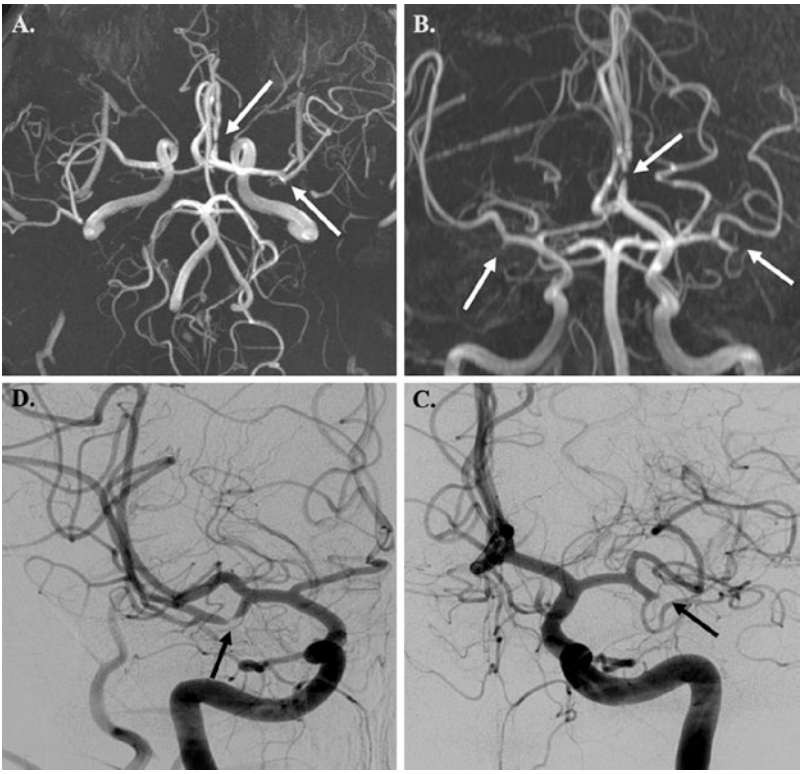

Fig. 2.8 (**a**) Axial 3D-TOF-MRA MIP shows occlusion of the inferior division of the left MCA and focal stenosis of the left A2 segment (arrows). (**b**) Coronal 3D-TOF-MRA MIP shows occlusion of the inferior divisions of the bilateral MCAs and high-grade left ACA stenosis (arrows). (**c**) Frontal DSA image of the left ICA demonstrates complete occlusion of the inferior division of the left MCA (arrow). (**d**) Frontal DSA image of the right ICA shows a high-grade, eccentric stenosis of the inferior division of the right MCA (arrow). MRA tends to overestimate the degree of luminal stenosis, as is evident in this case. Although the eccentric distribution of the stenosis is more commonly associated with ICAD, this patient had PCR-confirmed varicella-zoster virus (VZV) vasculitis

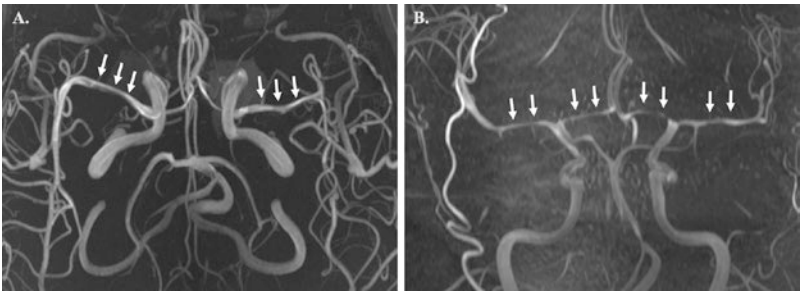

Fig. 2.9 (**a**) Axial 3D-TOF-MRA MIP image with diffuse narrowing of the bilateral M1 and proximal M2 segments (arrows). (**b**) Coronal 3D-TOF-MRA MIP image demonstrating severe diffuse narrowing of the bilateral M1 and A1 segments (arrows). This patient was found to have fungal meningitis complicated by severe vasculitis

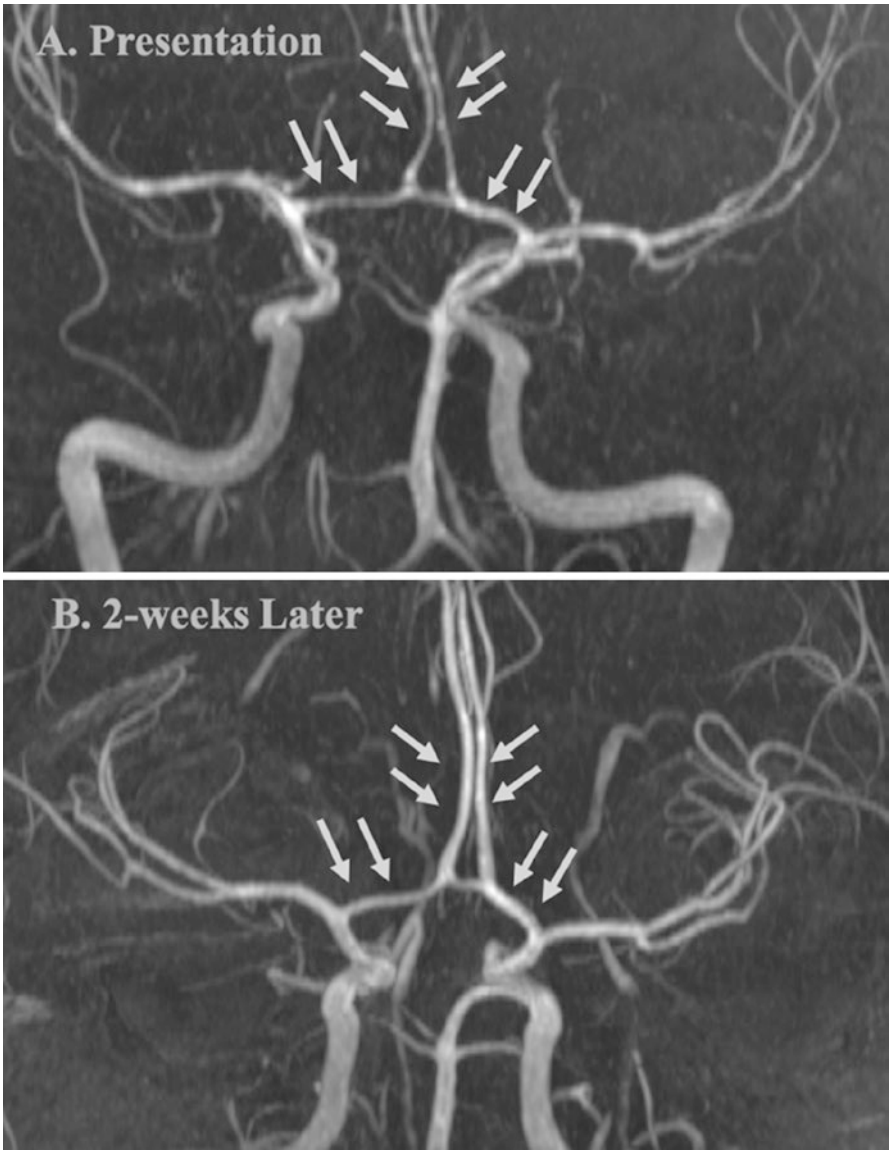

Fig. 2.10 (**a**) 3D-TOF-MRA demonstrates segmental narrowing of the bilateral A1 and A2 segments (arrows) at initial presentation. The affected arterial segments have a subtle beaded appearance. (**b**) Repeat MRA performed 2 weeks later illustrates marked improvement in vessel caliber (arrows). Although the luminal narrowing is nonspecific, the spontaneous improvement in the caliber of these arterial segments with time is consistent with reversible cerebral vasoconstriction syndrome (RCVS)

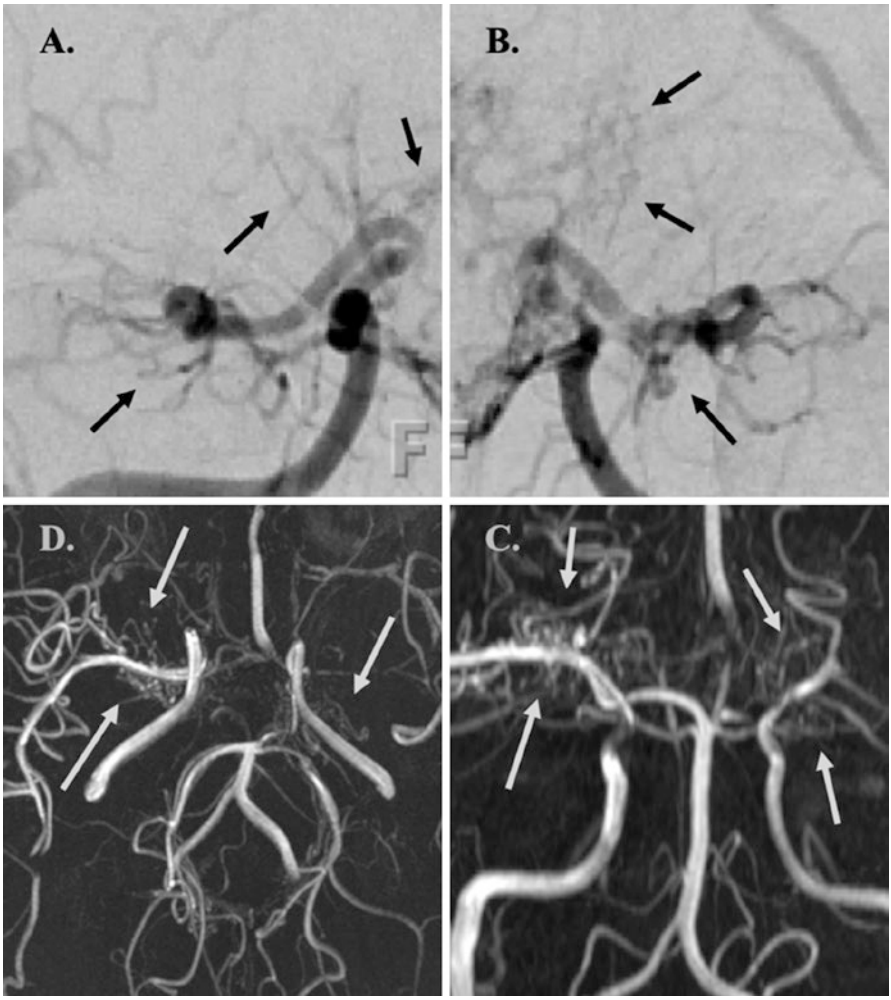

Fig. 2.11 (**a**, **b**) Frontal projection DSA images depicts steno-occlusive disease of the bilateral ICAs secondary to Moyamoya disease (MMD). There is occlusion of the terminal ICAs with development of robust compensatory basal ganglia perforators (arrows) giving the characteristic "puff of smoke" appearance associated with this disease process. (**c**, **d**) 3D-TOF-MRA MIP performed on a different patient again highlights steno-occlusive disease of the bilateral terminal ICAs with robust collateral vessel formation (arrows), compatible with MMD. MMD is a diagnosis of exclusion, reached only after other underlying vasculopathies are excluded. These include ICAD, infectious/inflammatory vasculopathy, or radiation-induced vasculopathy. If an underlying etiology for the luminal imaging abnormalities is identified, then a diagnosis of Moyamoya syndrome (MMS) is made. Unfortunately, luminal imaging has extreme difficulty discriminating between underlying vasculopathy etiologies

lopathy. However, these findings are not specific to any one disease process. The high spatial resolution of DSA allows for accurate evaluation of small peripheral arterial branches in addition to the circle of Willis and large proximal arterial segments [84, 87]. In cases of ICAD, the degree of luminal stenosis has proven helpful in predicting individual patient stroke risk [88, 89].

In most cases of intracranial vasculopathy, CTA and MRA will demonstrate segmental luminal narrowing of varying severity [84]. Although CT is sensitive to vascular calcifications, there is little impact of this finding in shaping one's differential diagnosis as these findings are most commonly related to senescence [90]. Multiple studies have demonstrated that it is difficult to confidently suggest an underlying etiology for multifocal intracranial stenoses based on luminal imaging findings alone [80, 81, 91] (Fig. 2.12). The accuracy of CTA in diagnosing ICAD has been reported to be less than 32%, whereas the accuracy with which it can diagnose intracranial vasculitis has been reported to be less than 15% [80].

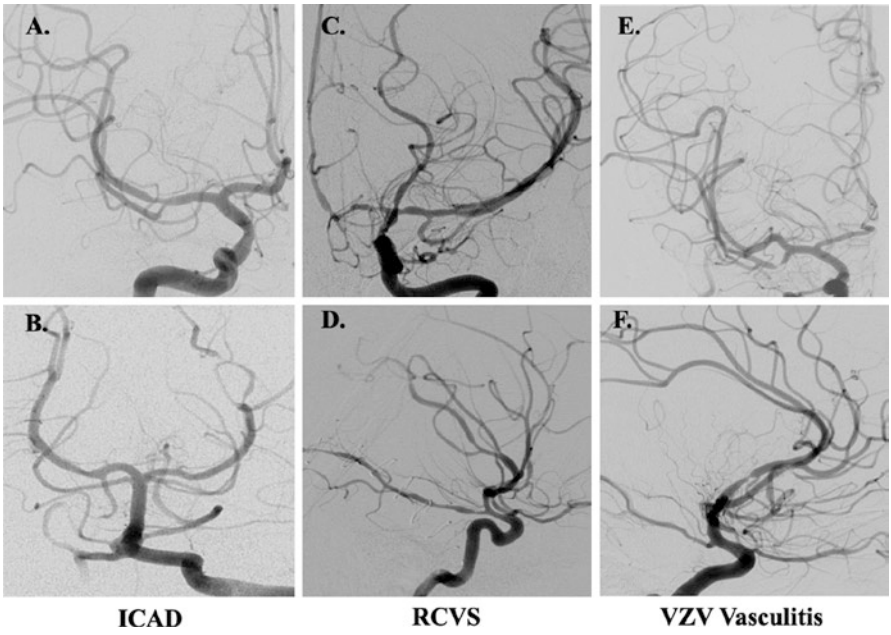

Fig. 2.12 (**a**, **b**) DSA images of the right ICA and posterior circulation, respectively, with multifocal luminal stenoses secondary to ICAD. (**c**, **d**) Oblique and lateral DSA images of the left ICA with multifocal stenoses secondary to RCVS. (**e**, **f**) Oblique and lateral DSA images of the left ICA with multifocal high-grade stenoses secondary to VZV vasculitis. Based on luminal imaging alone, it is nearly impossible to differentiate between these underlying etiologies. Advanced imaging techniques, such as dedicated MR vessel wall imaging (VWI), prove helpful in better differentiating causes for intracranial vasculopathy

Future Directions of Luminal Imaging

At present, luminal imaging provides limited information about the health of the vessel wall. Dedicated high spatial resolution vessel wall imaging (VWI) techniques that null intraluminal blood signal for improved vessel wall visualization may provide new insights into a multitude of cerebrovascular pathologies [92]. Moving forward, techniques that incorporate both luminal imaging and VWI acquisitions in the same sequence may prove to replace MR luminal imaging [91, 93–99]. Incorporation of VWI data into the luminal scan can help identify combinations of distinct imaging findings that can differentiate specific types of intracranial vasculopathies or better characterize disease risk [80, 81, 91, 100, 101].

Other new emerging imaging techniques will undoubtedly improve the quality of current luminal imaging. For instance, ultrashort echo time (UTE) MRA has the potential to reduce flow artifacts from turbulent flow and off-resonance artifacts from metallic implants [56]. In this technique, a short duration, spatially nonselective hard pulse for radiofrequency excitation, simultaneous gradient ramping and data acquisition, and k-space sampling with half radial projections are performed [56]. The development of simultaneous multislice (SMS) image acquisition techniques has the potential to accelerate image acquisition by a factor proportional to the number of slices/slabs simultaneously acquired [56, 102]. Incorporation of compressed sensing-sensitivity encoding (CS-SENSE) techniques, which rely on random undersampling of k-space, into MRA image acquisition algorithms represents another promising alternative for MRA acquisition acceleration that still preserves image quality [103]. The implementation of deep learning algorithms into imaging workflows and image processing has the potential to dramatically increase radiologist efficiency and image quality [56]. Implementation of intracranial artery feature extraction algorithms may provide quantitative vascular data that may better predict patient outcomes in the setting of intracranial vascular disease, including stroke and dementia [104].

References

1. Bechan RS, van Rooij SB, Sprengers ME, Peluso JP, Sluzewski M, Majoie CB, van Rooij WJ. CT angiography versus 3D rotational angiography in patients with subarachnoid hemorrhage. Neuroradiology. 2015;57(12):1239–46.
2. Chandra T, Pukenas B, Mohan S, Melhem E. Contrast-enhanced magnetic resonance angiography. Magn Reson Imaging Clin N Am. 2012;20(4):687–98.
3. Agid R, Andersson T, Almqvist H, Willinsky RA, Lee SK, ter Brugge KG, Farb RI, Soderman M. Negative CT angiography findings in patients with spontaneous subarachnoid hemorrhage: when is digital subtraction angiography still needed? AJNR Am J Neuroradiol. 2010;31(4):696–705.
4. Anderson GB, Ashforth R, Steinke DE, Findlay JM. CT angiography for the detection of cerebral vasospasm in patients with acute subarachnoid hemorrhage. AJNR Am J Neuroradiol. 2000;21(6):1011–5.

5. Aralasmak A, Akyuz M, Ozkaynak C, Sindel T, Tuncer R. CT angiography and perfusion imaging in patients with subarachnoid hemorrhage: correlation of vasospasm to perfusion abnormality. Neuroradiology. 2009;51(2):85–93.
6. Khosravani H, Mayer SA, Demchuk A, Jahromi BS, Gladstone DJ, Flaherty M, Broderick J, Aviv RI. Emergency noninvasive angiography for acute intracerebral hemorrhage. AJNR Am J Neuroradiol. 2013;34(8):1481–7.
7. Vogl TJ, Schulz B, Bauer RW, Stover T, Sader R, Tawfik AM. Dual-energy CT applications in head and neck imaging. AJR Am J Roentgenol. 2012;199(5 Suppl):S34–9.
8. Watanabe Y, Tsukabe A, Kunitomi Y, Nishizawa M, Arisawa A, Tanaka H, Yoshiya K, Shimazu T, Tomiyama N. Dual-energy CT for detection of contrast enhancement or leakage within high-density haematomas in patients with intracranial haemorrhage. Neuroradiology. 2014;56(4):291–5.
9. Dolati P, Eichberg D, Wong JH, Goyal M. The utility of dual-energy computed tomographic angiography for the evaluation of brain aneurysms after surgical clipping: a prospective study. World Neurosurg. 2015;84(5):1362–71.
10. Machida H, Tanaka I, Fukui R, Shen Y, Ishikawa T, Tate E, Ueno E. Dual-energy spectral CT: various clinical vascular applications. Radiographics. 2016;36(4):1215–32.
11. Deng K, Liu C, Ma R, Sun C, Wang XM, Ma ZT, Sun XL. Clinical evaluation of dual-energy bone removal in CT angiography of the head and neck: comparison with conventional bone-subtraction CT angiography. Clin Radiol. 2009;64(5):534–41.
12. Zhang LJ, Wu SY, Niu JB, Zhang ZL, Wang HZ, Zhao YE, Chai X, Zhou CS, Lu GM. Dual-energy CT angiography in the evaluation of intracranial aneurysms: image quality, radiation dose, and comparison with 3D rotational digital subtraction angiography. AJR Am J Roentgenol. 2010;194(1):23–30.
13. Zhang LJ, Wu SY, Poon CS, Zhao YE, Chai X, Zhou CS, Lu GM. Automatic bone removal dual-energy CT angiography for the evaluation of intracranial aneurysms. J Comput Assist Tomogr. 2010;34(6):816–24.
14. Alnemari A, Mansour TR, Bazerbashi M, Buehler M, Schroeder J, Gaudin D. Dynamic four-dimensional computed tomography angiography for neurovascular pathologies. World Neurosurg. 2017;105:1034 e1011-1034 e1018.
15. Kortman HG, Smit EJ, Oei MT, Manniesing R, Prokop M, Meijer FJ. 4D-CTA in neurovascular disease: a review. AJNR Am J Neuroradiol. 2015;36(6):1026–33.
16. Willems PW, Taeshineetanakul P, Schenk B, Brouwer PA, Terbrugge KG, Krings T. The use of 4D-CTA in the diagnostic work-up of brain arteriovenous malformations. Neuroradiology. 2012;54(2):123–31.
17. Smit EJ, Vonken EJ, Meijer FJ, Dankbaar JW, Horsch AD, van Ginneken B, Velthuis B, van der Schaaf I, Prokop M. Timing-invariant CT angiography derived from CT perfusion imaging in acute stroke: a diagnostic performance study. AJNR Am J Neuroradiol. 2015;36(10):1834–8.
18. Dehkharghani S, Bammer R, Straka M, Bowen M, Allen JW, Rangaraju S, Kang J, Gleason T, Brasher C, Nahab F. Performance of CT ASPECTS and collateral score in risk stratification: can target perfusion profiles be predicted without perfusion imaging? AJNR Am J Neuroradiol. 2016;37(8):1399–404.
19. Vagal A, Menon BK, Foster LD, Livorine A, Yeatts SD, Qazi E, d'Esterre C, Shi J, Demchuk AM, Hill MD, et al. Association between CT angiogram collaterals and CT perfusion in the interventional management of stroke III trial. Stroke. 2016;47(2):535–8.
20. van den Wijngaard IR, Boiten J, Holswilder G, Algra A, Dippel DW, Velthuis BK, Wermer MJ, van Walderveen MA. Impact of collateral status evaluated by dynamic computed tomographic angiography on clinical outcome in patients with ischemic stroke. Stroke. 2015;46(12):3398–404.
21. van Seeters T, Biessels GJ, Kappelle LJ, van der Schaaf IC, Dankbaar JW, Horsch AD, Niesten JM, Luitse MJ, Majoie CB, Vos JA, et al. CT angiography and CT perfusion improve prediction of infarct volume in patients with anterior circulation stroke. Neuroradiology. 2016;58(4):327–37.

22. Zhang S, Chen W, Tang H, Han Q, Yan S, Zhang X, Chen Q, Parsons M, Wang S, Lou M. The prognostic value of a four-dimensional CT angiography-based collateral grading scale for reperfusion therapy in acute ischemic stroke patients. PLoS One. 2016;11(8):e0160502.
23. Anzalone N, Scomazzoni F, Cirillo M, Righi C, Simionato F, Cadioli M, Iadanza A, Kirchin MA, Scotti G. Follow-up of coiled cerebral aneurysms at 3T: comparison of 3D time-of-flight MR angiography and contrast-enhanced MR angiography. AJNR Am J Neuroradiol. 2008;29(8):1530–6.
24. Ivancevic MK, Geerts L, Weadock WJ, Chenevert TL. Technical principles of MR angiography methods. Magn Reson Imaging Clin N Am. 2009;17(1):1–11.
25. Bremerich J, Bilecen D, Reimer P. MR angiography with blood pool contrast agents. Eur Radiol. 2007;17(12):3017–24.
26. Frydrychowicz A, Russe MF, Bock J, Stalder AF, Bley TA, Harloff A, Markl M. Comparison of gadofosveset trisodium and gadobenate dimeglumine during time-resolved thoracic MR angiography at 3T. Acad Radiol. 2010;17(11):1394–400.
27. Amarteifio E, Essig M, Bockler D, Attigah N, Schuster L, Demirel S. Comparison of gadofosveset (Vasovist((R))) with gadobenate dimeglumine (Multihance((R)))-enhanced MR angiography for high-grade carotid artery stenosis. J Neuroradiol. 2015;42(4):236–44.
28. Kau T, Gasser J, Celedin S, Rabitsch E, Eicher W, Uhl E, Hausegger KA. MR angiographic follow-up of intracranial aneurysms treated with detachable coils: evaluation of a blood-pool contrast medium. AJNR Am J Neuroradiol. 2009;30(8):1524–30.
29. Korosec FR, Frayne R, Grist TM, Mistretta CA. Time-resolved contrast-enhanced 3D MR angiography. Magn Reson Med. 1996;36(3):345–51.
30. Razek AA, Gaballa G, Megahed AS, Elmogy E. Time resolved imaging of contrast kinetics (TRICKS) MR angiography of arteriovenous malformations of head and neck. Eur J Radiol. 2013;82(11):1885–91.
31. Grist TM, Mistretta CA, Strother CM, Turski PA. Time-resolved angiography: past, present, and future. J Magn Reson Imaging. 2012;36(6):1273–86.
32. Lim RP, Shapiro M, Wang EY, Law M, Babb JS, Rueff LE, Jacob JS, Kim S, Carson RH, Mulholland TP, et al. 3D time-resolved MR angiography (MRA) of the carotid arteries with time-resolved imaging with stochastic trajectories: comparison with 3D contrast-enhanced Bolus-Chase MRA and 3D time-of-flight MRA. AJNR Am J Neuroradiol. 2008;29(10):1847–54.
33. Lim RP, Koktzoglou I. Noncontrast magnetic resonance angiography: concepts and clinical applications. Radiol Clin N Am. 2015;53(3):457–76.
34. Choi J, Seo H, Lim Y, Han Y, Park H. Sliding time of flight: sliding time of flight MR angiography using a dynamic image reconstruction method. Magn Reson Med. 2015;73(3):1177–83.
35. Miyazaki M, Akahane M. Non-contrast enhanced MR angiography: established techniques. J Magn Reson Imaging. 2012;35(1):1–19.
36. Kim HJ, Yoon DY, Kim ES, Lee HJ, Jeon HJ, Lee JY, Cho BM. Intraobserver and interobserver variability in CT angiography and MR angiography measurements of the size of cerebral aneurysms. Neuroradiology. 2017;59(5):491–7.
37. Dawkins AA, Evans AL, Wattam J, Romanowski CA, Connolly DJ, Hodgson TJ, Coley SC. Complications of cerebral angiography: a prospective analysis of 2,924 consecutive procedures. Neuroradiology. 2007;49(9):753–9.
38. Heit JJ, Pastena GT, Nogueira RG, Yoo AJ, Leslie-Mazwi TM, Hirsch JA, Rabinov JD. Cerebral angiography for evaluation of patients with CT angiogram-negative subarachnoid hemorrhage: An 11-year experience. AJNR Am J Neuroradiol. 2016;37(2):297–304.
39. Thiex R, Norbash AM, Frerichs KU. The safety of dedicated-team catheter-based diagnostic cerebral angiography in the era of advanced noninvasive imaging. AJNR Am J Neuroradiol. 2010;31(2):230–4.
40. Willinsky RA, Taylor SM, TerBrugge K, Farb RI, Tomlinson G, Montanera W. Neurologic complications of cerebral angiography: prospective analysis of 2,899 procedures and review of the literature. Radiology. 2003;227(2):522–8.

41. Citron SJ, Wallace RC, Lewis CA, Dawson RC, Dion JE, Fox AJ, Manzione JV, Payne CS, Rivera FJ, Russell EJ, et al. Quality improvement guidelines for adult diagnostic neuroangiography. Cooperative study between ASITN, ASNR, and SIR. J Vasc Interv Radiol. 2003;14(9 Pt 2):S257–62.
42. Brenner DJ, Hall EJ. Computed tomography--an increasing source of radiation exposure. N Engl J Med. 2007;357(22):2277–84.
43. Sodickson A, Baeyens PF, Andriole KP, Prevedello LM, Nawfel RD, Hanson R, Khorasani R. Recurrent CT, cumulative radiation exposure, and associated radiation-induced cancer risks from CT of adults. Radiology. 2009;251(1):175–84.
44. Cochran ST, Bomyea K, Sayre JW. Trends in adverse events after IV administration of contrast media. AJR Am J Roentgenol. 2001;176(6):1385–8.
45. McDonald JS, McDonald RJ, Carter RE, Katzberg RW, Kallmes DF, Williamson EE. Risk of intravenous contrast material-mediated acute kidney injury: a propensity score-matched study stratified by baseline-estimated glomerular filtration rate. Radiology. 2014;271(1):65–73.
46. McDonald JS, McDonald RJ, Tran CL, Kolbe AB, Williamson EE, Kallmes DF. Postcontrast acute kidney injury in pediatric patients: a cohort study. Am J Kidney Dis. 2018;72(6):811–8.
47. McDonald JS, McDonald RJ, Williamson EE, Kallmes DF, Kashani K. Post-contrast acute kidney injury in intensive care unit patients: a propensity score-adjusted study. Intensive Care Med. 2017;43(6):774–84.
48. McDonald RJ, McDonald JS, Bida JP, Carter RE, Fleming CJ, Misra S, Williamson EE, Kallmes DF. Intravenous contrast material-induced nephropathy: causal or coincident phenomenon? Radiology. 2013;267(1):106–18.
49. Davenport MS, Khalatbari S, Cohan RH, Dillman JR, Myles JD, Ellis JH. Contrast material-induced nephrotoxicity and intravenous low-osmolality iodinated contrast material: risk stratification by using estimated glomerular filtration rate. Radiology. 2013;268(3):719–28.
50. Davenport MS, Khalatbari S, Dillman JR, Cohan RH, Caoili EM, Ellis JH. Contrast material-induced nephrotoxicity and intravenous low-osmolality iodinated contrast material. Radiology. 2013;267(1):94–105.
51. Wallace RC, Karis JP, Partovi S, Fiorella D. Noninvasive imaging of treated cerebral aneurysms, part I: MR angiographic follow-up of coiled aneurysms. AJNR Am J Neuroradiol. 2007;28(6):1001–8.
52. Blackham KA, Passalacqua MA, Sandhu GS, Gilkeson RC, Griswold MA, Gulani V. Applications of time-resolved MR angiography. AJR Am J Roentgenol. 2011;196(5):W613–20.
53. Machet A, Portefaix C, Kadziolka K, Robin G, Lanoix O, Pierot L. Brain arteriovenous malformation diagnosis: value of time-resolved contrast-enhanced MR angiography at 3.0T compared to DSA. Neuroradiology. 2012;54(10):1099–108.
54. Zou Z, Ma L, Cheng L, Cai Y, Meng X. Time-resolved contrast-enhanced MR angiography of intracranial lesions. J Magn Reson Imaging. 2008;27(4):692–9.
55. Morita S, Masukawa A, Suzuki K, Hirata M, Kojima S, Ueno E. Unenhanced MR angiography: techniques and clinical applications in patients with chronic kidney disease. Radiographics. 2011;31(2):E13–33.
56. Edelman RR, Koktzoglou I. Noncontrast MR angiography: An update. J Magn Reson Imaging. 2019;49(2):355–73.
57. van Amerongen MJ, Boogaarts HD, de Vries J, Verbeek AL, Meijer FJ, Prokop M, Bartels RH. MRA versus DSA for follow-up of coiled intracranial aneurysms: a meta-analysis. AJNR Am J Neuroradiol. 2014;35(9):1655–61.
58. Agid R, Schaaf M, Farb R. CE-MRA for follow-up of aneurysms post stent-assisted coiling. Interv Neuroradiol. 2012;18(3):275–83.
59. Attali J, Benaissa A, Soize S, Kadziolka K, Portefaix C, Pierot L. Follow-up of intracranial aneurysms treated by flow diverter: comparison of three-dimensional time-of-flight MR angiography (3D-TOF-MRA) and contrast-enhanced MR angiography (CE-MRA) sequences with digital subtraction angiography as the gold standard. J Neurointerv Surg. 2016;8(1):81–6.

60. Boddu SR, Tong FC, Dehkharghani S, Dion JE, Saindane AM. Contrast-enhanced time-resolved MRA for follow-up of intracranial aneurysms treated with the pipeline embolization device. AJNR Am J Neuroradiol. 2014;35(11):2112–8.
61. Heit JJ, Gonzalez RG, Sabbag D, Brouwers HB, Ordonez Rubiano EG, Schaefer PW, Hirsch JA, Romero JM. Detection and characterization of intracranial aneurysms: a 10-year multidetector CT angiography experience in a large center. J Neurointerv Surg. 2016;8(11):1168–72.
62. Chen X, Liu Y, Tong H, Dong Y, Ma D, Xu L, Yang C. Meta-analysis of computed tomography angiography versus magnetic resonance angiography for intracranial aneurysm. Medicine (Baltimore). 2018;97(20):e10771.
63. Duarte Conde MP, de Korte AM, Meijer FJA, Aquarius R, Boogaarts HD, Bartels R, de Vries J. Subtraction CTA: An alternative imaging option for the follow-up of flow-diverter-treated aneurysms? AJNR Am J Neuroradiol. 2018;39(11):2051–6.
64. HaiFeng L, YongSheng X, YangQin X, Yu D, ShuaiWen W, XingRu L, JunQiang L. Diagnostic value of 3D time-of-flight magnetic resonance angiography for detecting intracranial aneurysm: a meta-analysis. Neuroradiology. 2017;59(11):1083–92.
65. Barreau X, Marnat G, Gariel F, Dousset V. Intracranial arteriovenous malformations. Diagn Interv Imaging. 2014;95(12):1175–86.
66. Grobovschek M, Himmer M, Wolfsgruber P, Weymayr F. Intracranial aneurysms and vascular malformations: diagnosis for therapy. A long-term study at a central hospital. A Neuroradiological approach. Part II: 2000-2008. The time of the beginning with newer diagnostic developments in CT, MR, DSA for endovascular intervention, microneurosurgery, radiotherapy. Neuroradiol J. 2011;24(6):889–94.
67. Spetzler RF, Martin NA. A proposed grading system for arteriovenous malformations. J Neurosurg. 1986;65(4):476–83.
68. Delgado Almandoz JE, Schaefer PW, Forero NP, Falla JR, Gonzalez RG, Romero JM. Diagnostic accuracy and yield of multidetector CT angiography in the evaluation of spontaneous intraparenchymal cerebral hemorrhage. AJNR Am J Neuroradiol. 2009;30(6):1213–21.
69. Derdeyn CP, Zipfel GJ, Albuquerque FC, Cooke DL, Feldmann E, Sheehan JP, Torner JC. Management of Brain Arteriovenous Malformations: a scientific statement for healthcare professionals from the American Heart Association/American Stroke Association. Stroke. 2017;48(8):e200–24.
70. Gross BA, Frerichs KU, Du R. Sensitivity of CT angiography, T2-weighted MRI, and magnetic resonance angiography in detecting cerebral arteriovenous malformations and associated aneurysms. J Clin Neurosci. 2012;19(8):1093–5.
71. Eddleman CS, Jeong HJ, Hurley MC, Zuehlsdorff S, Dabus G, Getch CG, Batjer HH, Bendok BR, Carroll TJ. 4D radial acquisition contrast-enhanced MR angiography and intracranial arteriovenous malformations: quickly approaching digital subtraction angiography. Stroke. 2009;40(8):2749–53.
72. Schubert T, Wu Y, Johnson KM, Wieben O, Maksimovic J, Mistretta C, Turski P. Time-of-arrival parametric maps and Virtual Bolus images derived from contrast-enhanced time-resolved radial magnetic resonance angiography improve the display of brain arteriovenous malformation vascular anatomy. Investig Radiol. 2016;51(11):706–13.
73. Reynolds MR, Lanzino G, Zipfel GJ. Intracranial Dural Arteriovenous Fistulae. Stroke. 2017;48(5):1424–31.
74. Gandhi D, Chen J, Pearl M, Huang J, Gemmete JJ, Kathuria S. Intracranial dural arteriovenous fistulas: classification, imaging findings, and treatment. AJNR Am J Neuroradiol. 2012;33(6):1007–13.
75. Lin YH, Wang YF, Liu HM, Lee CW, Chen YF, Hsieh HJ. Diagnostic accuracy of CTA and MRI/MRA in the evaluation of the cortical venous reflux in the intracranial dural arteriovenous fistula DAVF. Neuroradiology. 2018;60(1):7–15.
76. Nishimura S, Hirai T, Sasao A, Kitajima M, Morioka M, Kai Y, Omori Y, Okuda T, Murakami R, Fukuoka H, et al. Evaluation of dural arteriovenous fistulas with 4D contrast-enhanced MR angiography at 3T. AJNR Am J Neuroradiol. 2010;31(1):80–5.

77. Farb RI, Agid R, Willinsky RA, Johnstone DM, Terbrugge KG. Cranial dural arteriovenous fistula: diagnosis and classification with time-resolved MR angiography at 3T. AJNR Am J Neuroradiol. 2009;30(8):1546–51.
78. Mossa-Basha M, Wasserman BA. Low-grade carotid stenosis: implications of MR imaging. Neuroimaging Clin N Am. 2016;26(1):129–45.
79. Dieleman N, van der Kolk AG, van Veluw SJ, Frijns CJ, Harteveld AA, Luijten PR, Hendrikse J. Patterns of intracranial vessel wall changes in relation to ischemic infarcts. Neurology. 2014;83(15):1316–20.
80. Mossa-Basha M, de Havenon A, Becker KJ, Hallam DK, Levitt MR, Cohen WA, Hippe DS, Alexander MD, Tirschwell DL, Hatsukami T, et al. Added value of Vessel Wall magnetic resonance imaging in the differentiation of Moyamoya Vasculopathies in a non-Asian cohort. Stroke. 2016;47(7):1782–8.
81. Mossa-Basha M, Shibata DK, Hallam DK, de Havenon A, Hippe DS, Becker KJ, Tirschwell DL, Hatsukami T, Balu N, Yuan C. Added value of Vessel Wall magnetic resonance imaging for differentiation of nonocclusive intracranial Vasculopathies. Stroke. 2017;48(11):3026–33.
82. Bond KM, Nasr D, Lehman V, Lanzino G, Cloft HJ, Brinjikji W. Intracranial and Extracranial neurovascular manifestations of Takayasu arteritis. AJNR Am J Neuroradiol. 2017;38(4):766–72.
83. Mandell DM, Matouk CC, Farb RI, Krings T, Agid R, ter Brugge K, Willinsky RA, Swartz RH, Silver FL, Mikulis DJ. Vessel wall MRI to differentiate between reversible cerebral vasoconstriction syndrome and central nervous system vasculitis: preliminary results. Stroke. 2012;43(3):860–2.
84. Miller TR, Shivashankar R, Mossa-Basha M, Gandhi D. Reversible cerebral vasoconstriction syndrome, part 2: diagnostic work-up, imaging evaluation, and differential diagnosis. AJNR Am J Neuroradiol. 2015;36(9):1580–8.
85. Gounis MJ, van der Marel K, Marosfoi M, Mazzanti ML, Clarencon F, Chueh JY, Puri AS, Bogdanov AA Jr. Imaging inflammation in cerebrovascular disease. Stroke. 2015;46(10):2991–7.
86. Ahn SH, Lee J, Kim YJ, Kwon SU, Lee D, Jung SC, Kang DW, Kim JS. Isolated MCA disease in patients without significant atherosclerotic risk factors: a high-resolution magnetic resonance imaging study. Stroke. 2015;46(3):697–703.
87. Alexander MD, Cooke DL, Meyers PM, Amans MR, Dowd CF, Halbach VV, Higashida RT, Hetts SW. Lesion stability characteristics outperform degree of stenosis in predicting outcomes following stenting for symptomatic intracranial atherosclerosis. J Neurointerv Surg. 2016;8(1):19–23.
88. Chimowitz MI, Kokkinos J, Strong J, Brown MB, Levine SR, Silliman S, Pessin MS, Weichel E, Sila CA, Furlan AJ, et al. The Warfarin-Aspirin symptomatic intracranial disease study. Neurology. 1995;45(8):1488–93.
89. Kasner SE, Chimowitz MI, Lynn MJ, Howlett-Smith H, Stern BJ, Hertzberg VS, Frankel MR, Levine SR, Chaturvedi S, Benesch CG, et al. Predictors of ischemic stroke in the territory of a symptomatic intracranial arterial stenosis. Circulation. 2006;113(4):555–63.
90. Vos A, Van Hecke W, Spliet WG, Goldschmeding R, Isgum I, Kockelkoren R, Bleys RL, Mali WP, de Jong PA, Vink A. Predominance of nonatherosclerotic internal elastic Lamina calcification in the intracranial internal carotid artery. Stroke. 2016;47(1):221–3.
91. Mossa-Basha M, Hwang WD, De Havenon A, Hippe D, Balu N, Becker KJ, Tirschwell DT, Hatsukami T, Anzai Y, Yuan C. Multicontrast high-resolution vessel wall magnetic resonance imaging and its value in differentiating intracranial vasculopathic processes. Stroke. 2015;46(6):1567–73.
92. Lindenholz A, van der Kolk AG, Zwanenburg JJM, Hendrikse J. The use and pitfalls of intracranial vessel wall imaging: how we do it. Radiology. 2018;286(1):12–28.
93. Balu N, Zhou Z, Hippe DS, Hatsukami T, Mossa-Basha M, Yuan C. Accelerated multicontrast high isotropic resolution 3D intracranial vessel wall MRI using a tailored k-space undersampling and partially parallel reconstruction strategy. New York: Magma; 2019.

94. Chen S, Ning J, Zhao X, Wang J, Zhou Z, Yuan C, Chen H. Fast simultaneous noncontrast angiography and intraplaque hemorrhage (fSNAP) sequence for carotid artery imaging. Magn Reson Med. 2017;77(2):753–8.
95. Chen S, Zhao H, Li J, Zhou Z, Li R, Balu N, Yuan C, Chen H, Zhao X. Evaluation of carotid atherosclerotic plaque surface characteristics utilizing simultaneous noncontrast angiography and intraplaque hemorrhage (SNAP) technique. J Magn Reson Imaging. 2018;47(3):634–9.
96. Fan Z, Yu W, Xie Y, Dong L, Yang L, Wang Z, Conte AH, Bi X, An J, Zhang T, et al. Multicontrast atherosclerosis characterization (MATCH) of carotid plaque with a single 5-min scan: technical development and clinical feasibility. J Cardiovasc Magn Reson. 2014;16:53.
97. Li D, Zhao H, Chen X, Chen S, Qiao H, He L, Li R, Xu J, Yuan C, Zhao X. Identification of intraplaque haemorrhage in carotid artery by simultaneous non-contrast angiography and intraPlaque haemorrhage (SNAP) imaging: a magnetic resonance vessel wall imaging study. Eur Radiol. 2018;28(4):1681–6.
98. Qi H, Sun J, Qiao H, Chen S, Zhou Z, Pan X, Wang Y, Zhao X, Li R, Yuan C, et al. Carotid intraplaque hemorrhage imaging with quantitative vessel wall T1 mapping: technical development and initial experience. Radiology. 2018;287(1):276–84.
99. Shu H, Sun J, Hatsukami TS, Balu N, Hippe DS, Liu H, Kohler TR, Zhu W, Yuan C. Simultaneous noncontrast angiography and intraplaque hemorrhage (SNAP) imaging: comparison with contrast-enhanced MR angiography for measuring carotid stenosis. J Magn Reson Imaging. 2017;46(4):1045–52.
100. Lehman VT, Brinjikji W, Kallmes DF, Huston JR, Lanzino G, Rabinstein AA, Makol A, Mossa-Bosha M. Clinical interpretation of high-resolution vessel wall MRI of intracranial arterial diseases. Br J Radiol. 2016;89(1067):20160496.
101. Obusez EC, Hui F, Hajj-Ali RA, Cerejo R, Calabrese LH, Hammad T, Jones SE. High-resolution MRI vessel wall imaging: spatial and temporal patterns of reversible cerebral vasoconstriction syndrome and central nervous system vasculitis. AJNR Am J Neuroradiol. 2014;35(8):1527–32.
102. Schulz J, Boyacioglu R, Norris DG. Multiband multislab 3D time-of-flight magnetic resonance angiography for reduced acquisition time and improved sensitivity. Magn Reson Med. 2016;75(4):1662–8.
103. Vranic JE, Cross NM, Wang Y, Hippe DS, de Weerdt E, Mossa-Basha M. Compressed sensing-sensitivity encoding (CS-SENSE) accelerated brain imaging: reduced scan time without reduced image quality. AJNR Am J Neuroradiol. 2019;40(1):92–8.
104. Chen L, Mossa-Basha M, Sun J, Hippe DS, Balu N, Yuan Q, Pimentel K, Hatsukami TS, Hwang JN, Yuan C. Quantification of morphometry and intensity features of intracranial arteries from 3D TOF MRA using the intracranial artery feature extraction (iCafe): a reproducibility study. Magn Reson Imaging. 2019;57:293–302.